

**APPLICATION OF COMPUTATIONAL FLUID DYNAMICS  
ON A BLUNT ELLIPTICAL AIRFOIL**

by

Cristina Bhamburkar

---

A Thesis Submitted to the Faculty of the  
DEPARTMENT OF AEROSPACE AND MECHANICAL ENGINEERING

In Partial Fulfillment of the Requirements  
For the Degree of

MASTER OF SCIENCE  
WITH A MAJOR IN AEROSPACE ENGINEERING

In the Graduate College  
THE UNIVERSITY OF ARIZONA

Tucson, Arizona

2009

### STATEMENT BY AUTHOR

This thesis has been submitted in partial fulfillment of requirements for an advanced degree at The University of Arizona and is deposited in the University Library to be made available to borrowers under rules of the Library.

Brief quotations from this thesis are allowable without special permission, provided that accurate acknowledgment of source is made. Requests for permission for extended quotation from or reproduction of this manuscript in whole or in part may be granted by the head of the major department or the Dean of the Graduate College when in his or her judgment the proposed use of the material is in the interests of scholarship. In all other instances, however, permission must be obtained from the author.

SIGNED: \_\_\_\_\_

### APPROVAL BY THESIS DIRECTOR

This thesis has been approved on the date shown below:

---

Dr. Israel J. Wygnanski  
Professor of Aerospace Engineering

---

Date

## TABLE OF CONTENTS

NOMENCLATURE .....	5
ACKNOWLEDGEMENT .....	7
ABSTRACT .....	8
CHAPTER 1 INTRODUCTION .....	9
CHAPTER 2 BACKGROUND .....	10
2.1 Active Flow Control .....	10
2.2 Turbulence Modeling .....	10
2.3 Elliptical Airfoils .....	11
CHAPTER 3 THEORY .....	12
3.1 Solution Method .....	12
3.1.1 Governing Equations .....	12
3.1.2 Finite Volume Approach .....	15
3.2 Turbulence Model Equations .....	16
3.2.1 Equations of Motion .....	16
3.2.2 The Baldwin Lomax Model .....	18
3.2.3 One and Two Equation Models .....	19
3.2.4 The Spalart Allmaras Model .....	19
3.2.5 The Wilcox k-Omega Model .....	20
3.2.6 Menter's k-Omega SST Model .....	21
3.3 Time Advancement .....	22
3.4 Boundary Conditions .....	24
3.4.1 Extrapolation Boundary Condition .....	24
3.4.2 Viscous Surface Boundary Condition .....	24
3.4.3 Boundary Condition for Suction and Blowing .....	25
3.5 Convergence Acceleration .....	25
CHAPTER 4 PROCEDURE .....	27
4.1 Geometry .....	27
4.2 Grid Generation .....	27

4.3	CFD Software CFL3D .....	28
CHAPTER 4 RESULTS AND DISCUSSION .....		29
5.1	Baseline Flow .....	29
5.1.1	Velocity and Pressure Contours .....	30
5.1.2	Comparison of Trip Locations .....	33
5.1.3	Trailing Edge Cusp .....	34
5.2	Active Flow Control .....	39
5.2.1	Steady Suction and Blowing at Trailing Edge .....	39
5.2.2	Steady Suction at Leading Edge .....	47
5.3	Time Dependent Behavior Study .....	50
5.3.1	Varying Time Steps .....	51
5.3.2	Varying the Number of Subiterations .....	53
5.3.3	Issues with the Residuals .....	53
5.3.4	Issues for a Wide Variety of Physical Parameters .....	54
5.3.5	Baldwin-Lomax Solution .....	56
5.4	Turbulence Model Comparison .....	60
5.4.1	Unsteady Behavior .....	61
5.4.2	Power Spectrum Analysis .....	64
CHAPTER 6 CONCLUSION .....		68
BIBLIOGRAPHY .....		69

## NOMENCLATURE

$C_d$  = drag coefficient

$C_l$  = lift coefficient

$C_p$  = pressure coefficient

$C_\mu$  = momentum coefficient

$D$  = drag

$L$  = lift

$\alpha$  = angle of attack

$C$  = chord length

$h$  = slot width

$R$  = radius of the cylinders

$Re$  = Reynolds number

$M$  = Mach number

$St$  = Strouhal number

$\tilde{L}$  = characteristic length, meters

$L_{ref}$  = corresponding length in the grid, nondimensional

$\tilde{L}_R = \tilde{L} / L_{ref}$  = reference length used by the code, meters

$\tilde{a}$  = free stream speed of sound, meters/sec

$d\tilde{t}$  = time step, sec

$dt$  = time step, nondimensional

$p$  = pressure

$\rho$  = density

$\mu$  = molecular viscosity

$\lambda$  = bulk viscosity

$\Omega$  = vorticity

$Pr$  = Prandtl number

## ACRONYMS

CFD = Computational Fluid Dynamics

CFL3D = Computational Fluids Laboratory 3-Dimensional (Flow Solver)

MPI = Message Passing Interface

PLOT3D = Plot 3-Dimensional

TE = Trailing Edge

LE = Leading Edge

AOA = Angle of Attack

## **ACKNOWLEDGEMENT**

It is a pleasure to thank those who made this thesis possible. I would like to thank Dr. Israel J. Wygnanski for his guidance throughout my graduate studies and for helping me to develop an understanding of the subject. I would also like to thank Dr. Ahmed Hassan for his advice and help during this project.

I owe my deepest gratitude to my family for their support and understanding. Lastly, I offer my regards to all of those who supported me during the completion of the project

## ABSTRACT

Research was carried out in order to investigate the aerodynamics of a blunt elliptical airfoil with circular leading and trailing edges. A computational fluid dynamics (CFD) code was used to apply active flow control in the form of steady blowing and suction so as to enhance understanding of the physics of the airfoil. A Navier-Stokes CFD code called CFL3D developed at NASA Langley Research Center was used to perform the computations. Results obtained through CFD are then validated by comparing them to the group's internal results obtained experimentally at the Aerodynamics Laboratory at the University of Arizona. In order to model the turbulent flow field around the ellipse, four turbulence models were tested including the (1) Spalart-Allmaras turbulence model (2) Baldwin-Lomax turbulence model (3) Wilcox k-Omega turbulence model and (4) Menter's k-Omega turbulence model. The baseline flow at zero angle of attack was studied in depth and solutions were computed through post-stall angles. Physical parameters like the slot location, slot width, and momentum coefficient were varied. Also, CFD parameters like the time step and the number of subiterations were varied and optimized to obtain better solutions. This paper details the work done to validate the code on this model while studying a variety of CFD parameters and turbulence models.



## CHAPTER 1: INTRODUCTION

This paper attempts to validate CFL3D on the elliptical airfoil case based on the code's ability to predict (1) various methods of flow control (2) time averaged flow characteristics and (3) time dependent flow characteristics. Initially, the baseline flow predicted by CFL3D will be studied and parameters such as the lift and drag coefficients at varying angles of attack will be compared to lab results. The trip strip that is used on the experimental model will be simulated by applying a laminar-turbulent transition location with the model. Also, suction and blowing are applied at the leading edge and trailing edge near critical flow regions to study the codes ability to predict AFC's capabilities to delay/advance transition or prevent/provoke separation. Overall, it becomes clear that the code is well suited for computing the time averaged flow characteristics, especially the lift coefficient. It is also able to predict various flow phenomenon associated with AFC and yields results that are similar to lab results.

Lastly, the time dependent behavior of the code is studied and compared to theoretical expectations, since experimentally there were no time-dependent results for comparison. It was found that the time-dependent behavior is erratic and even the time-averaged values of some parameters such as the drag coefficient are heavily dependent on parameters such as time step and number of subiterations used within the code. It is also found that the various turbulence models yield scattered results. This is altogether not surprising, since it is known that turbulence models are often suited for a certain range of cases. So, it is concluded that the oscillatory wake behind the ellipse is likely outside the range of the Spallart-Allmaras model. Also, some observations are made for other turbulence models, though they are not studied in depth. It is found that the Baldwin-Lomax model and Menter's k-omega model do not exhibit the erratic behavior of the Spalart-Allmaras model, with solutions that do not depend so heavily on the time step or subiterations.

## **CHAPTER 2: BACKGROUND**

### **2.1 Active Flow Control**

Ludwig Prandtl first used active flow control to influence boundary layers in the early 1900's. Through his experiments, he showed how AFC applied to the boundary layer can have a great influence on the flow. Experiments in the 60's and 70's made use of unsteady flow visualizations. In the 80's and 90's experiments on turbulent flows like jets, wakes, and mixing layers showed the potential of AFC as a major research field. Currently, AFC is used to alter the natural flow to a more desirable flow pattern, to reduce drag, increase lift and control separation. There are many types of passive and active flow control, including wing flaps, slats, strips, suction, and blowing. Currently, there are both computational and experimental efforts to determine and optimize the parameters governing active flow control.

### **2.2 Turbulence Modeling**

In 1877, Boussinesq first suggested that turbulent shear stress correlated to eddy viscosity and made the first step in determining how turbulence influences flows. Later, Prandtl's (1925) mixing length hypothesis was the first algebraic model of turbulence. From the 1940's through the 1970's there was a the further development of algebraic, one and two equation turbulence models. Currently, for all RANS or URANS computations at high Reynolds numbers, turbulence models are required. However, there is much debate about the accuracy of the results for time-dependent flows. Many of the models are validated (or calibrated) for specific cases of flow problems, and turn out to be inadequate when the flow conditions are outside the model's specific range. So, no turbulence model is universally accepted. However, the most successful models include the Baldwin-Lomax, Baldwin-Barth, Spalart-Allmaras, and k-Omega models.

## 2.3 Elliptical Airfoils

An elliptical airfoil model has been tested in the subsonic wind tunnel at the Aerodynamics Laboratory at the University of Arizona. Blunt bodies such as the elliptical airfoil have been tested and found to have large wakes and highly oscillatory behavior. As a computational model, the ellipse should be similar to the circular cylinder in subsonic flow. (Figure 1) Namely, the trailing edge of the ellipse has the same curve as the trailing edge of the circular cylinder. However, while the behavior of the circular cylinder is well predicted by CFL3D using the Spalart-Allmaras turbulence model, the behavior of the ellipse not well predicted. In fact, the behavior predicted by the Spalart-Allmaras model is found to be heavily dependent on parameters within the code such as the time step and number of subiterations.

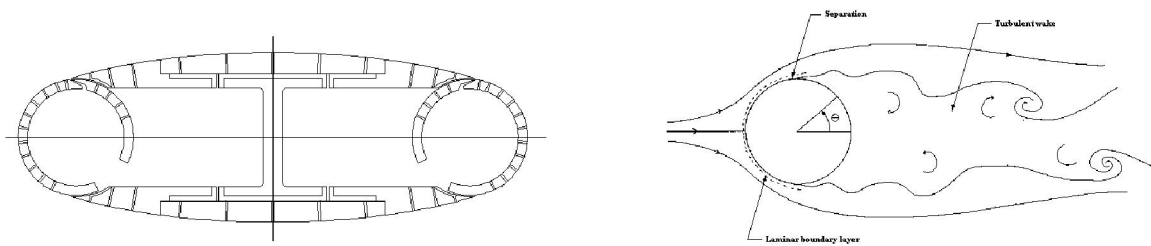


**Figure 1: A geometric comparison of the elliptical airfoil to a circular cylinder**

## CHAPTER 3: THEORY

### 3.1 Solution Method

#### 3.1.1 Governing Equations

The governing equations used in CFL3D are given in the CFL3D Version 5 Manual. They are thin-layer approximations to the three dimensional time dependent compressible Navier-Stokes equations. They can be written in terms of the generalized coordinates  $(\xi, \eta, \zeta)$  as shown in equation 1.

$$\frac{\partial \hat{\mathbf{Q}}}{\partial t} + \frac{\partial (\hat{\mathbf{F}} - \hat{\mathbf{F}}_v)}{\partial \xi} + \frac{\partial (\hat{\mathbf{G}} - \hat{\mathbf{G}}_v)}{\partial \eta} + \frac{\partial (\hat{\mathbf{H}} - \hat{\mathbf{H}}_v)}{\partial \zeta} = 0 \quad (1)$$

A transformation between the Cartesian variables  $(x, y, z)$  and the generalized coordinates  $(\xi, \eta, \zeta)$  of the grid is implied. The variable  $J$  represents the Jacobian of the transformation from  $(x, y, z)$  to  $(\xi, \eta, \zeta)$ .

$$J = \frac{\partial(\xi, \eta, \zeta, t)}{\partial(x, y, z, t)} \quad (2)$$

In equation 1,  $\hat{\mathbf{Q}}$  is the vector of the variables including density, momentum, and total energy per unit volume.

$$\hat{\mathbf{Q}} = \frac{\mathbf{Q}}{J} = \frac{1}{J} \begin{bmatrix} \rho \\ \rho \cdot u \\ \rho \cdot v \\ \rho \cdot w \\ e \end{bmatrix} \quad (3)$$

The inviscid flux terms are

$$\hat{\mathbf{F}} = \frac{\mathbf{F}}{J} = \frac{1}{J} \begin{bmatrix} \rho U \\ \rho U u + \xi_x p \\ \rho U v + \xi_y p \\ \rho U w + \xi_z p \\ (e + p)U - \xi_t p \end{bmatrix} \quad (4)$$

$$\hat{\mathbf{G}} = \frac{\mathbf{G}}{J} = \frac{1}{J} \begin{bmatrix} \rho V \\ \rho V u + \eta_x p \\ \rho V v + \eta_y p \\ \rho V w + \eta_z p \\ (e + p)V - \eta_t p \end{bmatrix} \quad (5)$$

$$\hat{\mathbf{H}} = \frac{\mathbf{H}}{J} = \frac{1}{J} \begin{bmatrix} \rho W \\ \rho W u + \zeta_x p \\ \rho W v + \zeta_y p \\ \rho W w + \zeta_z p \\ (e + p)W - \zeta_t p \end{bmatrix} \quad (6)$$

The viscous flux terms are

$$\hat{\mathbf{F}}_v = \frac{\mathbf{F}_v}{J} = \frac{1}{J} \begin{bmatrix} 0 \\ \xi_x \tau_{xx} + \xi_y \tau_{xy} + \xi_z \tau_{xz} \\ \xi_x \tau_{xy} + \xi_y \tau_{yy} + \xi_z \tau_{yz} \\ \xi_x \tau_{xz} + \xi_y \tau_{yz} + \xi_z \tau_{zz} \\ \xi_x b_x + \xi_y b_y + \xi_z b_z \end{bmatrix} \quad (7)$$

$$\hat{\mathbf{G}}_v = \frac{\mathbf{G}_v}{J} = \frac{1}{J} \begin{bmatrix} 0 \\ \eta_x \tau_{xx} + \eta_y \tau_{xy} + \eta_z \tau_{xz} \\ \eta_x \tau_{xy} + \eta_y \tau_{yy} + \eta_z \tau_{yz} \\ \eta_x \tau_{xz} + \eta_y \tau_{yz} + \eta_z \tau_{zz} \\ \eta_x b_x + \eta_y b_y + \eta_z b_z \end{bmatrix} \quad (8)$$

$$\hat{\mathbf{H}}_v = \frac{\mathbf{H}_v}{J} = \frac{1}{J} \begin{bmatrix} 0 \\ \zeta_x \tau_{xx} + \zeta_y \tau_{xy} + \zeta_z \tau_{xz} \\ \zeta_x \tau_{xy} + \zeta_y \tau_{yy} + \zeta_z \tau_{yz} \\ \zeta_x \tau_{xz} + \zeta_y \tau_{yz} + \zeta_z \tau_{zz} \\ \zeta_x b_x + \zeta_y b_y + \zeta_z b_z \end{bmatrix} \quad (9)$$

Now, recognize that equation 1 represents the conservation equations. The five equations are one equation for the conservation of mass, three equations for the conservation of momentum along each coordinate direction, and one equation for the conservation of energy. In these equations, the shear stress and heat flux terms are defined in tensor notation.

$$\tau_{x_i x_j} = \frac{M}{\text{Re}} \left[ \mu \left( \frac{\partial u_i}{\partial x_j} + \frac{\partial u_j}{\partial x_i} \right) + \lambda \frac{\partial u_k}{\partial x_k} \delta_{ij} \right] \quad (10)$$

$$b_{x_i} = u_j \tau_{x_i x_j} - \frac{q_{x_i}}{\text{Pr}} \quad (11)$$

$$q_{x_i} = - \left[ \frac{M_\infty \mu}{\text{Re Pr}(\gamma - 1)} \right] \frac{\partial a^2}{\partial x_i} \quad (12)$$

The pressure is obtained by the equation of state for a perfect gas.

$$p = (\gamma - 1) \left[ e - \frac{\rho}{2} (u^2 + v^2 + w^2) \right] \quad (13)$$

These equations are nondimensionalized in terms of the free-stream density,  $\tilde{\rho}_\infty$ , speed of

sound,  $\tilde{a}_\infty$ , and molecular viscosity,  $\tilde{\mu}_\infty$ . In order to apply the thin-layer approximation, only the derivatives in the direction normal to the wall ( $\zeta$ ) are included in the shear stress and heat flux terms. Equation 10 is closed by the Stokes hypothesis for bulk viscosity ( $\lambda + 2\mu/3 = 0$ ) and Sutherland's law for molecular viscosity.

### 3.1.2 Finite Volume Approach

CFL3D uses a finite-volume formulation, resulting in an approximation to the conservation laws in integral form

$$\frac{\partial}{\partial t} \iiint_V \mathbf{Q} dV + \iint_S \mathbf{f} \cdot \mathbf{n} dS = 0 \quad (14)$$

$\mathbf{f}$  denotes the net flux through a surface  $S$  with unit normal  $\mathbf{n}$  containing the volume  $V$ . Integration of Equation 14 over a control volume bounded by lines of constant  $\xi$ ,  $\eta$ , and  $\zeta$  along the grid lines gives the following form

$$\begin{aligned} \left( \frac{\partial \hat{\mathbf{Q}}}{\partial t} \right)_{i,j,k} &+ (\hat{\mathbf{F}} - \hat{\mathbf{F}}_v)_{i+1/2,j,k} - (\hat{\mathbf{F}} - \hat{\mathbf{F}}_v)_{i-1/2,j,k} \\ &+ (\hat{\mathbf{G}} - \hat{\mathbf{G}}_v)_{i,j+1/2,k} - (\hat{\mathbf{G}} - \hat{\mathbf{G}}_v)_{i,j-1/2,k} \\ &+ (\hat{\mathbf{H}} - \hat{\mathbf{H}}_v)_{i,j,k+1/2} - (\hat{\mathbf{H}} - \hat{\mathbf{H}}_v)_{i,j,k-1/2} = 0 \end{aligned} \quad (15)$$

The values  $\hat{\mathbf{Q}}_{i,j,k}$  are regarded as average values taken over a unit grid cell. Also, the values of  $\hat{\mathbf{F}}$ ,  $\hat{\mathbf{G}}$ , and  $\hat{\mathbf{H}}$  are regarded as face-average values.

## 3.2 Turbulence Model Equations

### 3.2.1 Equations of Motion

Favre averaging can be used with the Navier-Stokes equations to account for turbulent fluctuations. The resulting equations of motion can be written using the summation convention as follows. The full Navier-Stokes equations are shown here, but in CFL3D, they are solved as the thin-layer approximation in pre-selected coordinate direction(s). The  $\sim$  indicates a dimensional quantity.

$$\frac{\partial \tilde{\rho}}{\partial \tilde{t}} + \frac{\partial}{\partial \tilde{x}_j} (\tilde{\rho} \tilde{u}_j) = 0 \quad (16)$$

$$\frac{\partial}{\partial \tilde{t}} (\tilde{\rho} \tilde{u}_i) + \frac{\partial}{\partial \tilde{x}_j} (\tilde{\rho} \tilde{u}_j \tilde{u}_i) = -\frac{\partial \tilde{p}}{\partial \tilde{x}_i} + \frac{\partial \tilde{\tau}_{ji}}{\partial \tilde{x}_j} \quad (17)$$

$$\frac{\partial}{\partial \tilde{t}} (\tilde{\rho} \tilde{E}) + \frac{\partial}{\partial \tilde{x}_j} (\tilde{\rho} \tilde{u}_j \tilde{H}) = \frac{\partial}{\partial \tilde{x}_j} [\tilde{u}_i \tilde{\tau}_{ij} - \tilde{\Phi}_j + \tilde{\Psi}_j] \quad (18)$$

where

$$\tilde{p} = (\gamma - 1) \left[ \tilde{\rho} \tilde{E} - \frac{1}{2} \tilde{\rho} (\tilde{u}^2 + \tilde{v}^2 + \tilde{w}^2) \right] \quad (19)$$

$$\tilde{E} = \tilde{e} + \frac{1}{2} (\tilde{u}^2 + \tilde{v}^2 + \tilde{w}^2) \quad (20)$$

$$\tilde{H} = \tilde{E} + \frac{\tilde{p}}{\tilde{\rho}} \quad (21)$$

$$\tilde{\Phi}_j = -\frac{1}{\gamma - 1} \left( \frac{\tilde{\mu}}{\text{Pr}} + \frac{\tilde{\mu}_T}{\text{Pr}_T} \right) \frac{\partial \tilde{a}^2}{\partial \tilde{x}_j} \quad (22)$$

$$\tilde{a}^2 = \frac{\gamma \cdot \tilde{p}}{\tilde{\rho}} \quad (23)$$

Next, define



$$\tilde{S}_{ij} = \frac{1}{2} \left( \frac{\partial \tilde{u}_i}{\partial \tilde{x}_j} + \frac{\partial \tilde{u}_j}{\partial \tilde{x}_i} \right) \quad (24)$$

$$\tilde{W}_{ij} = \frac{1}{2} \left( \frac{\partial \tilde{u}_i}{\partial \tilde{x}_j} - \frac{\partial \tilde{u}_j}{\partial \tilde{x}_i} \right) \quad (25)$$

The magnitude of vorticity is

$$\tilde{\Omega} = \sqrt{2\tilde{W}_{ij}\tilde{W}_{ij}} \quad (26)$$

The shear stress  $\tilde{\tau}_{ij}$  term is composed of laminar and turbulent components

$$\tilde{\tau}_{ij} = \tilde{\tau}_{ij}^L + \tilde{\tau}_{ij}^T \quad (27)$$

where

$$\tilde{\tau}_{ij}^L = 2\tilde{\mu} \left( \tilde{S}_{ij} - \frac{1}{3} \frac{\partial \tilde{u}_k}{\partial \tilde{x}_k} \delta_{ij} \right) \quad (28)$$

Also, for all eddy-viscosity models in CFL3D the following approximations are made. In this paper, all the models tested are all eddy viscosity models.

$$\tilde{\tau}_{ij}^T = 2\tilde{\mu}_T \left( \tilde{S}_{ij} - \frac{1}{3} \frac{\partial \tilde{u}_k}{\partial \tilde{x}_k} \delta_{ij} \right) \quad (29)$$

$$\tilde{\Psi}_j = 0 \quad (30)$$

The Navier-Stokes equations are nondimensionalized and written in generalized coordinates, as described previously. For eddy-viscosity models, the end result is that the turbulent Navier-Stokes equations are identical to the laminar equations with the exception that

$\tilde{\mu}$  is replaced by  $\tilde{\mu} + \tilde{\mu}_T$

and

$$\frac{\tilde{\mu}}{\text{Pr}} \text{ is replaced by } \frac{\tilde{\mu}}{\text{Pr}} + \frac{\tilde{\mu}_T}{\text{Pr}_T}$$

$\tilde{\mu}_T$  is the eddy viscosity value obtained by the turbulence model that is used. Also, it is assumed that  $\text{Pr} = 0.72$  and  $\text{Pr}_T = 0.9$ .

### 3.2.2 The Baldwin-Lomax Model

The Baldwin-Lomax model is an algebraic model. Because it is the original model employed in CFL3D, its implementation is different from the one and two equation models. For the Baldwin-Lomax model,

$$\begin{aligned} \mu_T &= \mu_{T,inner} & y &\leq y_{crossover} \\ \mu_T &= \mu_{T,outer} & y &> y_{crossover} \end{aligned}$$

where  $y_{crossover}$  is the location along the constant grid line where  $\mu_{T,inner}$  exceeds  $\mu_{T,outer}$ , while marching away from the wall. The inner and outer eddy viscosities are given by

$$\mu_{T,inner} = \rho l^2 \Omega \left( \frac{\text{Re}}{M_\infty} \right) \quad (31)$$

$$\mu_{T,outer} = 0.0168(1.6) \rho F_{wake} F_{kleb} \left( \frac{\text{Re}}{M} \right) \quad (32)$$

where, for the inner eddy viscosity,

$$l = y [1 - \exp(-y^+ / 26)] \quad (33)$$

$$y^+ = \frac{\sqrt{\rho\tau_w}}{\mu} y \left( \frac{\text{Re}}{M_\infty} \right)^{1/2} \quad (34)$$

and, for the outer eddy viscosity,

$$F_{wake} = \min \left[ y_{\max} F_{\max}, 1.0 y_{\max} u_{dif}^2 / F_{\max} \right] \quad (35)$$

$$F(y) = y \Omega [1 - \exp(-y^+ / 26)] \quad (36)$$

$$F_{kleb} = \left[ 1 + 5.5 \left( \frac{0.3y}{y_{\max}} \right)^6 \right]^{-1} \quad (37)$$

$$u_{dif} = \left( \sqrt{u^2 + v^2 + w^2} \right)_{\max} - \left( \sqrt{u^2 + v^2 + w^2} \right)_{\min} \quad (38)$$

The second term in  $u_{dif}$  is taken to be zero. In wakes,  $\exp(-y^+ / 26)$  is set to zero.  $F_{\max}$  is the maximum value of  $F(y)$  that occurs in a profile and  $y_{\max}$  is the value at which  $F_{\max}$  occurs.

### 3.2.3 One and Two Equation Models

The one and two equation models can be written in the general form

$$\frac{\partial}{\partial t}(X) + u_j \frac{\partial}{\partial x_j}(X) = S_p + S_D + D \quad (39)$$

$S_p$  is a “production” source term,  $S_D$  is a “destruction” source term, and  $D$  is a diffusion term. All of the field equation models are solved uncoupled from the Navier-Stokes equations in a similar fashion using this equation. Also, all of the one and two equation models are based on incompressible turbulence equations. No compressibility corrections have been added.

### 3.2.4 The Spalart-Allmaras Model

The Spalart-Allmaras model solves a single field equation for a variable  $\hat{v}$ , which is

related to the eddy viscosity  $\mu_T$  through

$$\mu_T = \rho \hat{v} f_{v1} \quad (40)$$

For the general form in equation 39

$$\begin{aligned} X &= \hat{v} \\ S_p &= C_{b1} [1 - f_{t2}] \Omega \hat{v} \\ S_D &= \frac{M_\infty}{\text{Re}} \left\{ C_{b1} [(1 - f_{t2}) f_{v2} + f_{t2}] \frac{1}{\kappa^2} - C_{w1} f_w \right\} \left( \frac{\hat{v}}{d} \right)^2 \\ D &= -\frac{M_\infty}{\text{Re}} \frac{C_{b2}}{\sigma} \hat{v} \frac{\partial^2 \hat{v}}{\partial x_i^2} + \frac{M_\infty}{\text{Re}} \frac{1}{\sigma} \frac{\partial}{\partial x_j} \left[ (v + (1 + C_{b2}) \hat{v}) \frac{\partial \hat{v}}{\partial x_j} \right] \end{aligned} \quad (41)$$

In these equations,  $d$  is called the minimum distance function. It is the distance to the nearest viscous wall. The variables  $C_{b1}$ ,  $C_{w1}$ ,  $C_{b2}$ ,  $\kappa$ , and  $\sigma$  are constants, while the variables  $f_{t2}$ ,  $f_{v2}$ ,  $f_w$ , and  $f_{v1}$  are all functions of the variable  $\hat{v}$  and other constants.

### 3.2.5 The Wilcox k-Omega Model

The Wilcox k-Omega Model is a two-equation models which solves for the variables  $k$  and  $\omega$  in order to compute the value of the eddy viscosity  $\mu_T$  to use in the governing equations. In this model,

$$\mu_T = \frac{\rho k}{\omega} \quad (42)$$

For the general form in equation 39

$$X_k = k \quad (43)$$

$$\begin{aligned}
S_{P,k} &= \frac{1}{\rho} \mu_T \Omega^2 \left( \frac{M_\infty}{\text{Re}} \right) \\
S_{D,k} &= -\beta' k \omega \left( \frac{\text{Re}}{M_\infty} \right) \\
D_k &= \frac{1}{\rho} \frac{\partial}{\partial x_j} \left[ \left( \mu + \frac{\mu_T}{\sigma_k} \right) \frac{\partial k}{\partial x_j} \right] \left( \frac{M_\infty}{\text{Re}} \right)
\end{aligned}$$

and

$$\begin{aligned}
X_\omega &= \omega \tag{44} \\
S_{P,\omega} &= \gamma \Omega^2 \left( \frac{M_\infty}{\text{Re}} \right) \\
S_{D,\omega} &= -\beta \omega^2 \left( \frac{\text{Re}}{M_\infty} \right) \\
D_\omega &= \frac{1}{\rho} \frac{\partial}{\partial x_j} \left[ \left( \mu + \frac{\mu_T}{\sigma_\omega} \right) \frac{\partial \omega}{\partial x_j} \right] \left( \frac{M_\infty}{\text{Re}} \right)
\end{aligned}$$

In these equations  $\beta$ ,  $\beta'$ ,  $\sigma_k$ ,  $\sigma_\omega$ , and  $\gamma$  are constants.

### 3.2.6 Menter's k-Omega SST Model

Menter's k-Omega Model is a two-equation models which solves for the variables  $k$  and  $\omega$  in order to compute the value of the eddy viscosity  $\mu_T$  and is similar to the Wilcox model. However in this model, the eddy viscosity is defined as the minimum of two different functions.

$$\mu_T = \min \left[ \frac{\rho k}{\omega}, \frac{a_1 \rho k}{\Omega F_2} \left( \frac{\text{Re}}{M} \right) \right] \tag{45}$$

For the general form in equation 39, the Menter k-Omega SST model is equivalent to the

Wilcox model, except for the term  $S_{D,\omega}$ , which is given by

$$S_{D,\omega} = -\beta\omega^2 \left( \frac{\text{Re}}{M_\infty} \right) + 2(1 - F_1)\sigma_{\omega 2} \frac{1}{\omega} \frac{\partial k}{\partial x_j} \frac{\partial \omega}{\partial x_j} \left( \frac{M_\infty}{\text{Re}} \right) \quad (46)$$

$F_1$  is similar to equation 45 because it chooses the minimum of several functions of  $k$  and  $\omega$ . Also,  $\sigma_{\omega 2}$  is a constant.

### 3.3 Time Advancement

For a structured grid that cannot be deformed, equation 1 can be written as

$$\frac{1}{J} \frac{\partial \mathbf{Q}}{\partial t} = R(\mathbf{Q}) \quad (47)$$

where

$$R = - \left[ \frac{\partial (\hat{\mathbf{F}} - \hat{\mathbf{F}}_v)}{\partial \xi} + \frac{\partial (\hat{\mathbf{G}} - \hat{\mathbf{G}}_v)}{\partial \eta} + \frac{\partial (\hat{\mathbf{H}} - \hat{\mathbf{H}}_v)}{\partial \zeta} \right] \quad (48)$$

The time term can be discretized with backward differencing

$$\frac{(1 + \phi)(\mathbf{Q}^{n+1} - \mathbf{Q}^n) - \phi(\mathbf{Q}^n - \mathbf{Q}^{n-1})}{J\Delta t} = R(\mathbf{Q}^{n+1}) \quad (49)$$

The superscripts indicate time level. When  $\phi = 0$  the method is first-order temporally accurate; when  $\phi = 1/2$  the method is second-order accurate. This equation is implicit because the right-hand side is a function of the unknown flow variables at time level  $n + 1$ .

Because of the method which the left-hand side is treated for computational efficiency in steady-state simulations (first-order accuracy), second-order temporal accuracy is forfeited for

unsteady computations. One method for recovering the desired accuracy is through the use of sub-iterations. The sub-iteration strategy implemented in CFL3D is termed “pseudo time sub-iteration” ( $\tau$ -TS).

For the  $\tau$ -TS method, a pseudo time term is added to the time-accurate Navier-Stokes equations.

$$\frac{1}{J} \frac{\partial \mathbf{Q}}{\partial \tau} + \frac{(1+\phi)(\mathbf{Q}^{n+1} - \mathbf{Q}^n) - \phi(\mathbf{Q}^n - \mathbf{Q}^{n-1})}{J\Delta t} = R(\mathbf{Q}^{n+1}) \quad (50)$$

This equation is then discretized and iterated in  $m$ , where  $m$  is the subiteration counter.

$$\frac{(1+\phi')(\mathbf{Q}^{m+1} - \mathbf{Q}^m) - \phi'(\mathbf{Q}^m - \mathbf{Q}^{m-1})}{J\Delta \tau} + \frac{(1+\phi)(\mathbf{Q}^{m+1} - \mathbf{Q}^n) - \phi(\mathbf{Q}^n - \mathbf{Q}^{n-1})}{J\Delta t} = R(\mathbf{Q}^{m+1}) \quad (51)$$

In equation 51,  $\phi$  and  $\phi'$  govern the order of accuracy of the physical and pseudo time terms, respectively. In practice, the pseudo time term is treated as first order (i.e.,  $\phi' = 0$ ), but the general form is shown here for completeness. As  $m \rightarrow \infty$ , the pseudo time term vanishes if the sub-iterations converge and  $\mathbf{Q}^{m+1} \rightarrow \mathbf{Q}^{n+1}$ . The quantity  $\Delta \tau$  is based on a constant CFL number set by the input parameter  $dt$ .

The right hand side of the equation  $R(\mathbf{Q}^m)$  is output from CFL3D as a measure of the residual along with the lift and drag coefficients. This residual can then be used to evaluate the convergence of the solution.  $R(\mathbf{Q}^m)$  is a vector quantity so only the first term of  $R(\mathbf{Q}^m)$  (density) is output. This is equivalent to the residual of the mass conservation equation and is usually around  $10^{-8}$  for steady solutions and  $10^{-5}$  for unsteady solutions in CFL3D. Throughout this paper, the number that is often reported is the base 10 log of the residual.

### 3.4 Boundary Conditions

#### 3.4.1 Extrapolation Boundary Condition

The extrapolation boundary conditions are cell-center boundary conditions. The ghost points are extrapolated from the computational domain. Based on the locations of  $\rho_1$ ,  $\rho_{-1}$ , and  $\rho_{-2}$  depicted in Figure 2, the extrapolated values would be

$$\rho_{-1} = \rho_1$$

$$\rho_{-2} = \rho_1$$

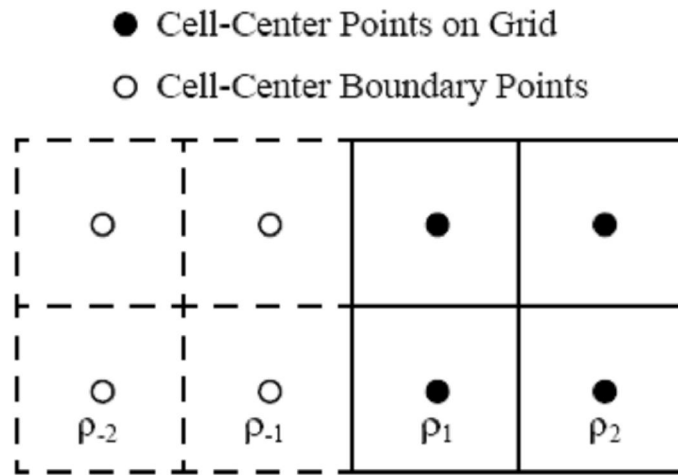


Figure 2: Extrapolation Boundary Condition Diagram

The same extrapolation is used for the boundary values of the other four flowfield variables.

#### 3.4.2 Viscous Surface Boundary Condition

The viscous surface boundary conditions are cell-face boundary conditions. The no-slip condition ( $V = 0$ ) is applied at the surface. Additional information on the wall temperature ( $\tilde{T}_w / \tilde{T}_\infty$ ) must also be supplied. The wall for ellipse case was set to be an adiabatic wall.



### 3.4.3 Boundary Condition for Suction and Blowing

The boundary condition for suction and blowing is an extension of the viscous wall boundary condition. However, there can now be inflow or outflow through the wall, with the coefficient  $C_q = (\rho u_{normal}) / (\rho u)_\infty$ . For suction,  $C_q$  is negative. And with this boundary condition the direction of the suction and blowing can be specified. The quantities **sjetx**, **sjety**, **sjetz** are the direction numbers of the blowing or suction in the x, y, and z directions. In the ellipse case several methods of blowing and suction are used. It is assumed that the blowing and suction cannot be applied perfectly tangent to the surface of the ellipse, so in CFL3D the blowing/suction is applied at a 30 degree angle to the surface.

### 3.5 Convergence Acceleration

For unsteady cases, second-order temporal accuracy is sacrificed for computational efficiency. However, second-order accuracy can be recovered by using sub-iterations. In this case, the computation was run second order accurate in time using the pseudo time sub-iteration ( -TS) method. Using this method, the greater the number sub-iterations, the more accurate the computation.

As shown in Figure 3, one can increase the accuracy of computations by increasing the number of sub-iterations (*ncyc*), decreasing the time step (*dt*), or increasing the grid size. So, for a given case, if different values of *ncyc* and *dt* are tested, the cases with the highest *ncyc* and lowest *dt* should be the most accurate. Generally, when performing analysis, some compromise is usually made between accuracy and efficiency. However, one criterion to limit the time step sizing is that the time scale must be small enough to resolve the real flow phenomenon that may oscillate at some frequency. So, very large time steps are not expected to be accurate.

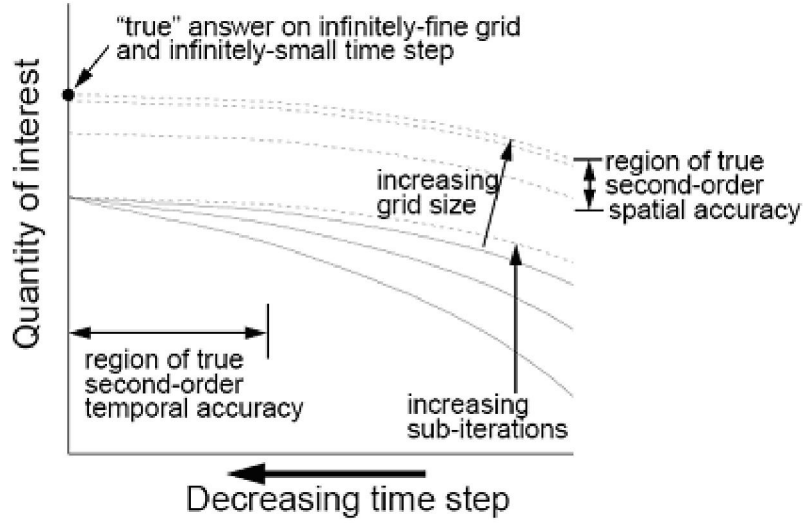


Figure 3: Dependence of time accuracy on  $dt$ ,  $nyc$ , and grid size

In the turbulence model study, the models are usually run with  $dt = 0.1$ , for consistency. However, the two k-omega models were not robust enough to generate solutions at this value of  $dt$ . So, these models were run at  $dt = 0.01$ . Also,  $dt$  is varied over two orders of magnitude (between 0.01 and 1.00) to study the effect of changing the time step. For these cases, the relationship between the nondimensional time step  $dt$  utilized in the code and it's corresponding physical time step,  $d\tilde{t}$  is given by equation 52. For these cases cases,  $\tilde{L} = 0.27127m$ ,  $L_{ref} = 1$ ,  $\tilde{L}_R = 0.27127m$ ,  $\tilde{a} = 341$  m/s, and  $dt$  is varied. Table 1 gives some values for  $dt$  and the corresponding values of  $d\tilde{t}$ .

$$dt = \frac{d\tilde{t} * \tilde{a}_{\infty}}{\tilde{L}_R} \quad (52)$$

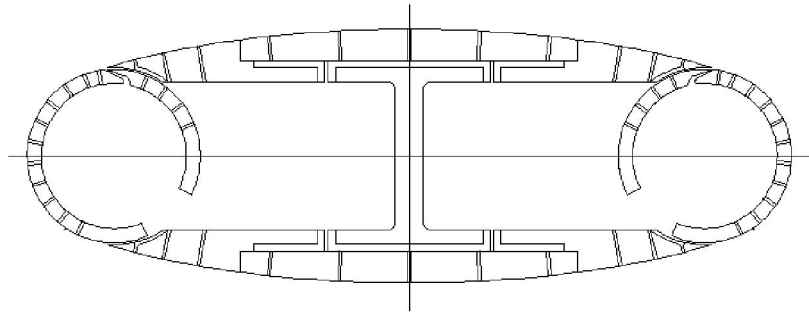
$dt$	0.01	0.05	0.10	0.50	1.00
$d\tilde{t}$ (sec)	$8*10^{-6}$	$4*10^{-5}$	$8*10^{-5}$	$4*10^{-4}$	$8*10^{-4}$

Table 1: Time step  $dt$  and corresponding values of  $d\tilde{t}$

## CHAPTER 4 PROCEDURE

### 4.1 Geometry

Although wind tunnel experiments are not performed in this thesis, internal results from the Aerodynamics Laboratory are used for comparison with CFD results. A 2D elliptical airfoil model with circular leading and trailing edges at zero angle of attack is used in all computations. Below is a diagram of the wind tunnel model of this airfoil (Figure 4). At both ends of this airfoil, circular cylinders are fitted with slots. The cylinders can be rotated and the slot widths can be varied to allow for various locations and methods of flow control. The chord length of the airfoil in the lab is approximately 27cm. During wind tunnel tests, a trip strip was set at 3cm (11% chord) on the upper and lower surfaces of the airfoil.



**Figure 4: Diagram of the elliptical airfoil**

### 4.2 Grid Generation

Using the Overgrid graphical user interface, a C-grid was built with dimensions 529 streamwise x 97 normal x 2 span-wise (Figure 5). There are 91 streamwise points in the wake, which extends a distance 20 times the chord length. The grid is split in the streamwise direction into 8 grid blocks to allow for computation in parallel mode. The individual grid blocks have dimensions 67x97x2. Although the case is 2D, CFL3D is a finite volume code requiring a 3D grid, so 2 grid points must be defined in the span-wise direction. Outside the grid in the span-

wise direction, a boundary condition is set up to extrapolate ghost points outside the flowfield domain (Figure 5).

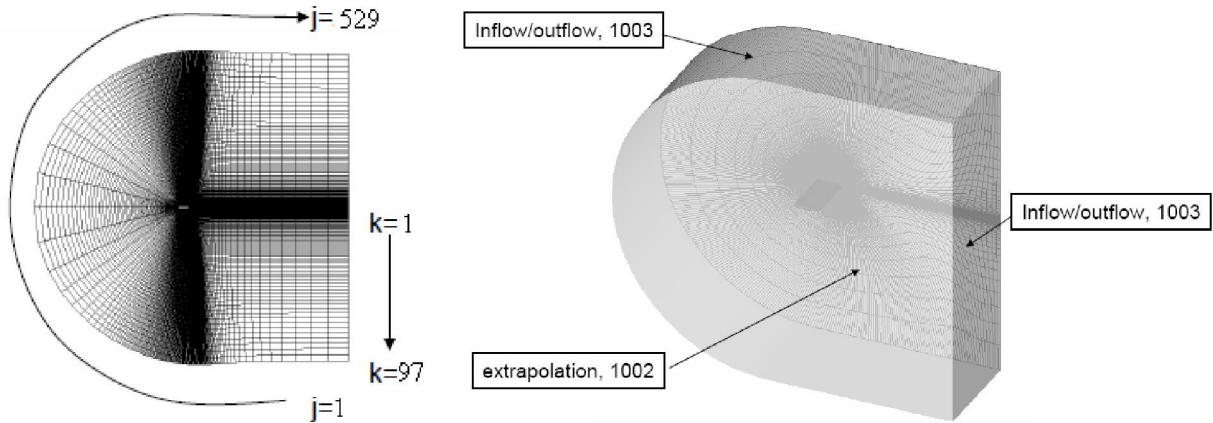


**Figure 5: Outer boundary conditions for a C-grid**

### 4.3 CFD Software CFL3D

Results are computed using CFL3D Version 6.4, a Reynolds-averaged thin-layer Navier-Stokes computational fluid dynamics code for structured grids. The spatial discretization uses a finite-volume approach. The implicit time advancement can solve steady and unsteady flows. Weiss-Smith low Mach number preconditioning is also implemented. The code is parallelized with Message Passing Interface (MPI) protocol. Also, the code offers numerous turbulence models. Four models have been tested, including Baldwin-Lomax, Spalart-Allmaras, Wilcox  $k$ - $\omega$ , and Menter SST  $k$ - $\omega$ . For all the cases under consideration, the Mach number was approximately 0.05 and the Reynolds number was 300,000.

## CHAPTER 5 RESULTS AND DISCUSSION

### 5.1 Baseline Flow

Figure 6 shows the pressure coefficient on the surface of the ellipse computed in CFL3D at zero angle of attack. It is plotted alongside experimental results obtained from the wind tunnel at the Aerodynamics Laboratory. From the figure it is clear that the predicted pressure coefficient is similar to the experimentally obtained pressure coefficient. What is most similar is the general shape of the curve, especially at the trailing edge where the pressure coefficient reaches a low negative constant value. The main differences are that the CFD results slightly underestimate the value of the pressure coefficient across much of the surface. Also, CFD results predict a greater spike in the pressure coefficient near the leading edge than in the experimental results, which predicts smoother values of the pressure coefficient near the leading edge.

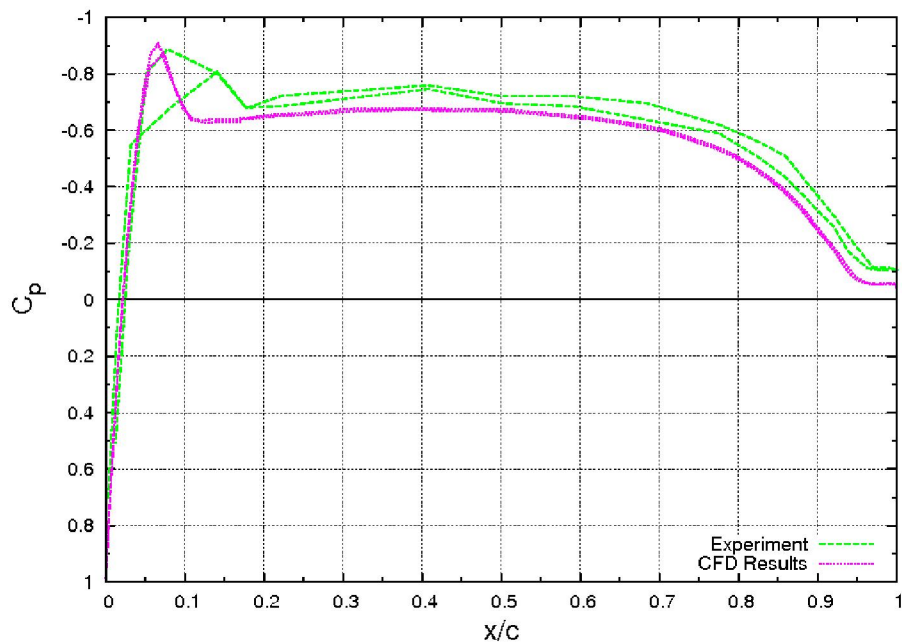
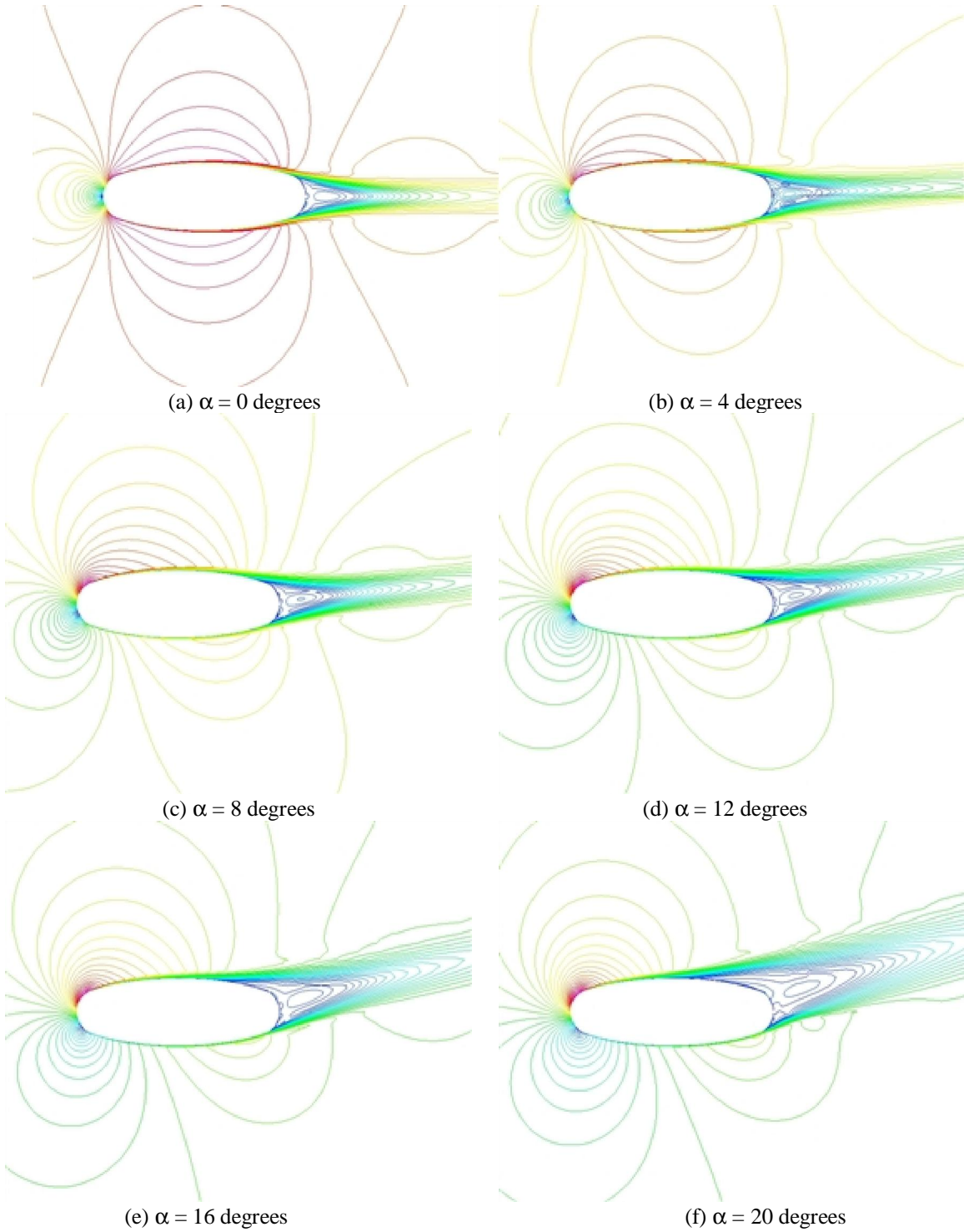


Figure 6:  $C_p$  vs.  $x/c$  for the ellipse at zero angle of attack

### 5.1.1 Velocity and Pressure Contours

Figure 7 shows the velocity contours for the ellipse for varying angles of attack ranging from 0 to 20 degrees. The contour lines represent lines of constant velocity magnitude. Figure 8 shows the pressure contours. In the velocity contour plots the red lines represent high velocity, while the blue lines indicate a low (near zero) velocity. Low velocities appear at the stagnation point at the leading edge, and in the wake close to the body. High velocities are most prevalent along the upper surface and near the leading edge of the ellipse. In the pressure contour plots red lines indicate low pressure regions, such as at the stagnation point and in the wake. Blue lines represent high pressure at the same location on the upper surface as the low velocity region.



**Figure 7: Velocity contours for ellipse at 0, 8, 12, 16, and 20 degrees**

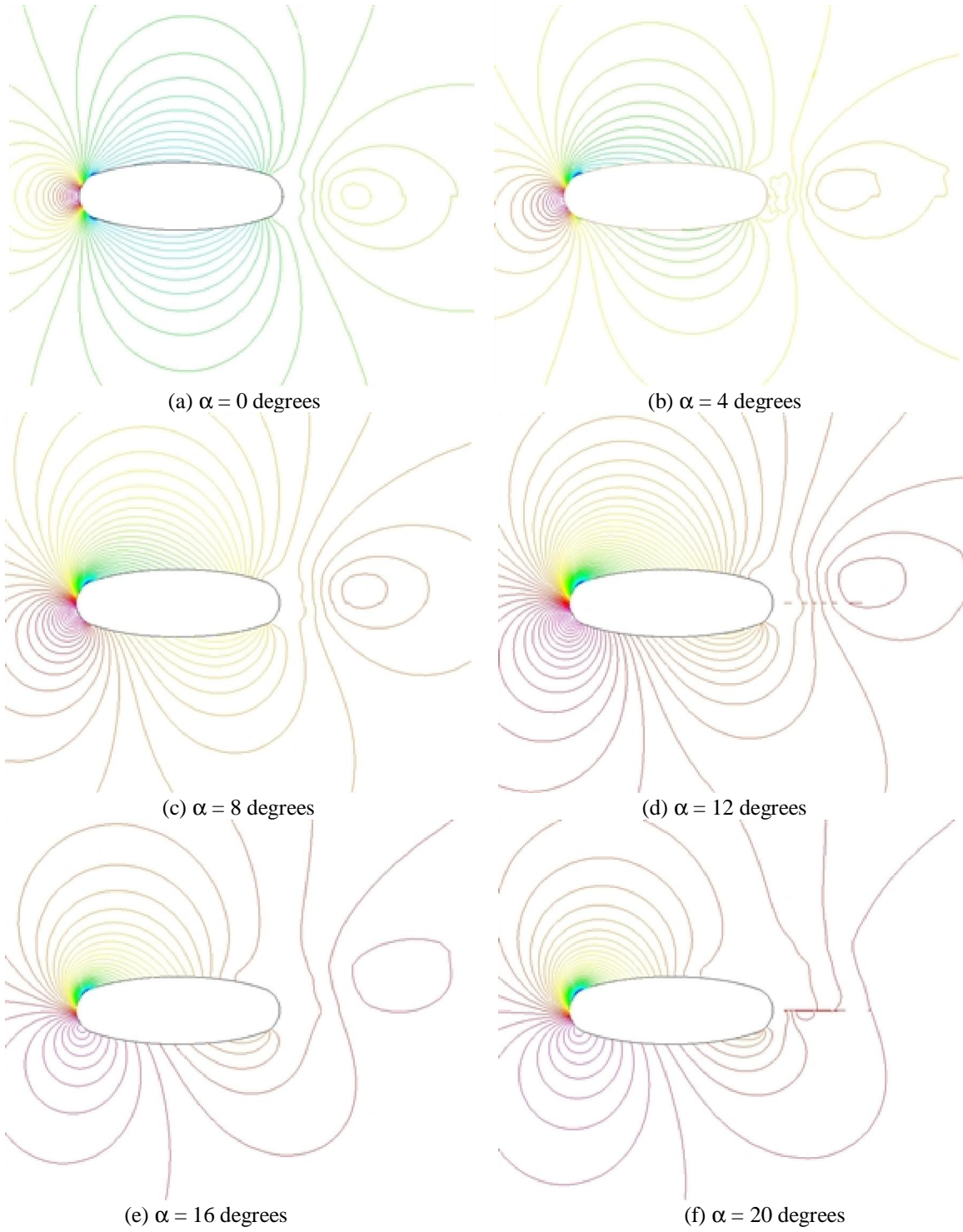
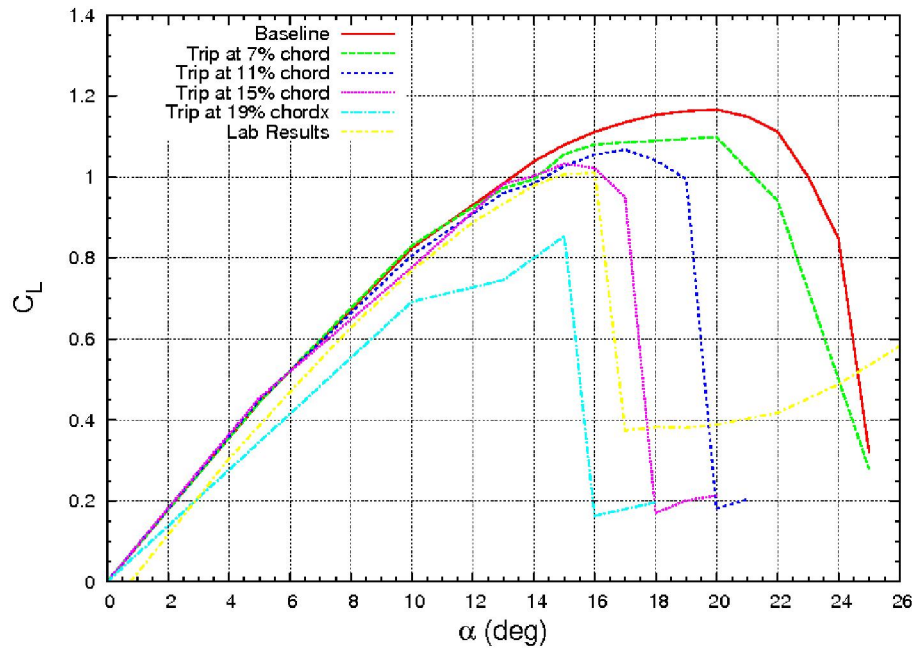


**Figure 8: Pressure contours for ellipse at 4, 8, 12, 16, and 20 degrees**



### 5.1.2 Comparison of trip locations

Next, a trip is simulated by defining a laminar region at the leading edge of the airfoil. The leading edge was forced to maintain a laminar boundary layer up to some percentage of the chord on the upper and lower surfaces. So, the grid points near the leading edge of the ellipse are run laminar (turbulent terms turned “off”), while the grid points near the trailing edge were run turbulent. Using this method, a laminar-turbulent transition location is simulated at varying locations, namely at 7%, 11%, 15%, and 19% of the chord length. In the lab, the ellipse had a trip strip at 11% chord. Figure 9 shows plots of  $C_L$  vs.  $\alpha$  and  $C_D$  vs.  $C_L$  for varying angles of attack for the ellipse with varying trip locations.



(a)

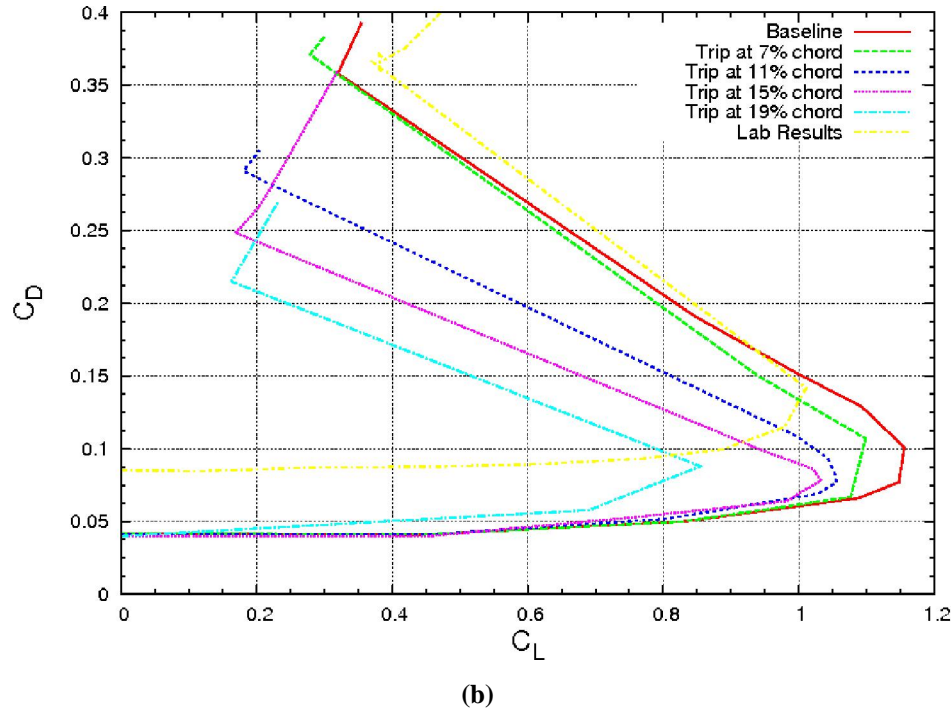


**Figure 9:  $C_L$  vs.  $\alpha$  and  $C_D$  vs  $C_L$  for the ellipse, Spalart-Allmaras Model**

Figure 9 shows that as the transition location is moved downstream, the angle of attack at which stall occurs is decreased. This earlier stall is characteristic of the actual behavior of the ellipse in the lab. So, it is concluded that the fully turbulent baseline solution is not necessarily the best solution, and that the results are better when a laminar-turbulent transition location is applied. From figure 9(a) it is clear that the transition location at 15% chord gives a stall angle that is near the stall angle of the experimental results. And, when a trip strip is used, the actual transition location is usually downstream of the trip strip. So, the results are consistent because the transition location downstream of the trip strip is most similar to lab results.

### 5.1.3 Trailing Edge Cusp

In order to reduce the size of the wake and study an alternate configuration for the ellipse, a cusp was added to the trailing edge of the ellipse. This cusp enforces the Kutta condition and drastically changes the behavior of the airfoil. The length of the triangular attachment is approximately 3.69'' and the two sides of the triangle make a 38 degree angle. A diagram of this attachment to the ellipse is shown in Figure 10.

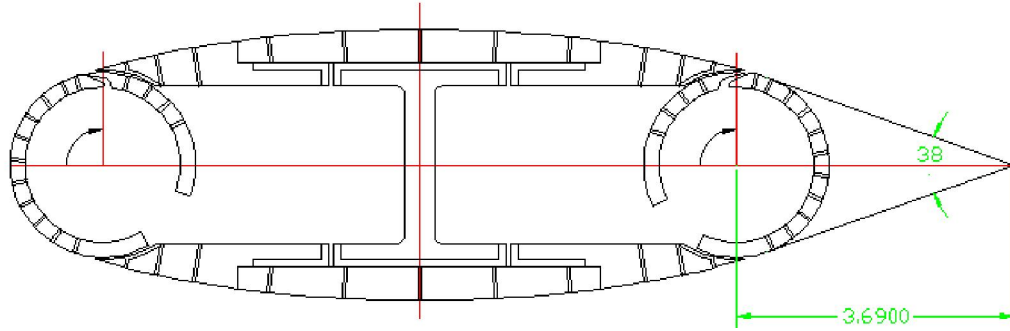


**Figure 10: Diagram of the Ellipse with the Cusp Attachment**

The pressure coefficient at the surface was plotted and is shown in Figure 11. The shape of this curve is very different from Figure 6 for the ellipse without the cusp. So, it is clear that the ellipse with the cusp exhibits very different behavior from the ellipse without one. The most notable difference is the pressure coefficient near the trailing edge. Without the cusp, the pressure coefficient at this location was negative. Now, with the cusp the pressure coefficient has considerably increased and is positive. Again, from this figure it is clear that the CFD results are very close to the experimental results. However, again, the behavior is slightly different at the leading edge of the ellipse near the trip location.

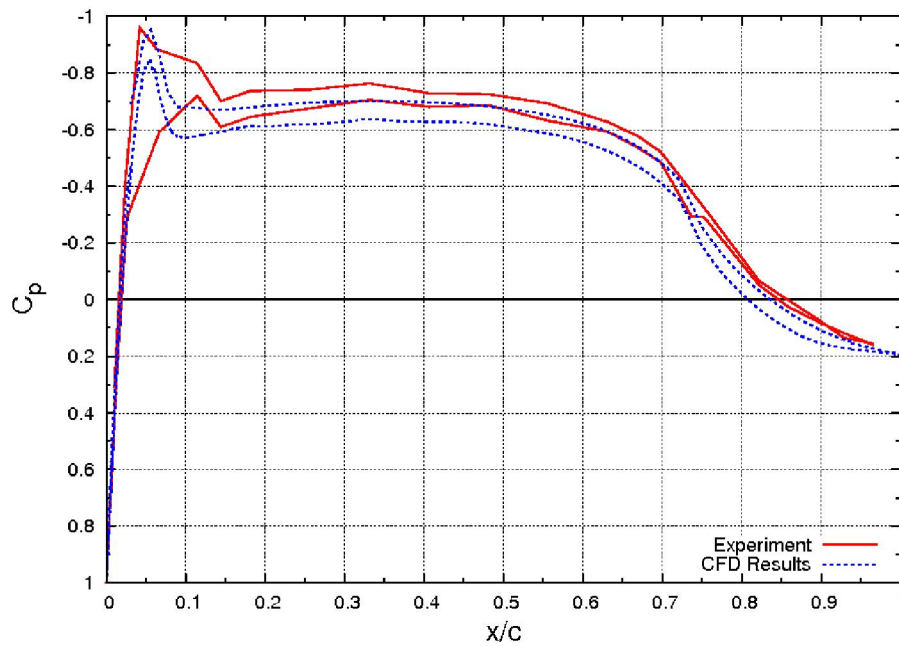


**Figure 6:  $C_p$  vs.  $x/c$  for the ellipse with a cusp at zero angle of attack**

Next, the ellipse with the cusp was run at varying angles of attack. Figure 12 shows  $C_L$  vs.  $\alpha$  for varying angles of attack for the ellipse with the cusp and the basic ellipse. From the plot it is clear that at small angles of attack there is a negative lift. This is due to the thickness ratio and the trailing edge angle. When the airfoil is rotated, the boundary layer switches from one side to the other. The growth at the upper surface and the suction of the attached flow at the lower surface are so strong that it produces a negative lift-curve slope. This negative lift is not observed with the elliptical section, so it can be concluded that the sharp trailing edge is necessary to produce this negative slope.

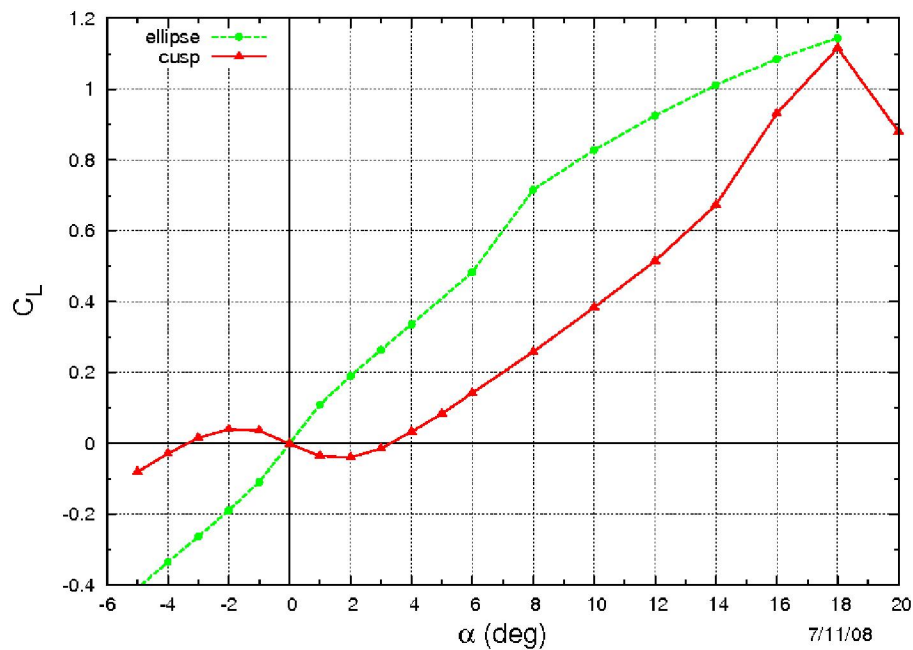
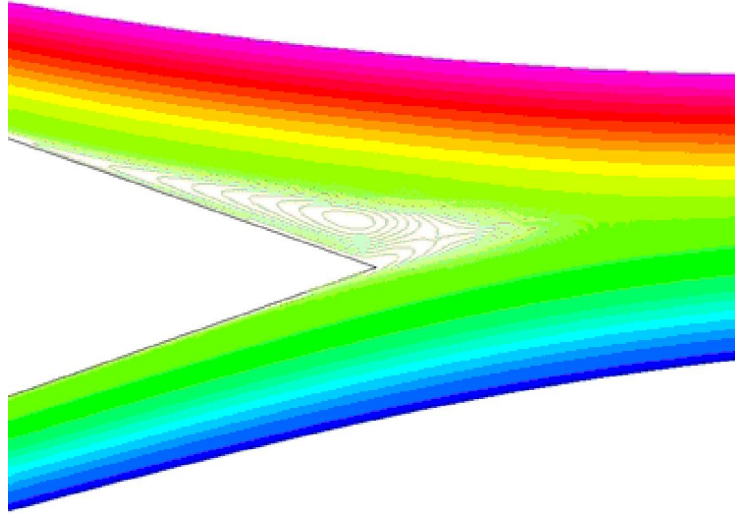
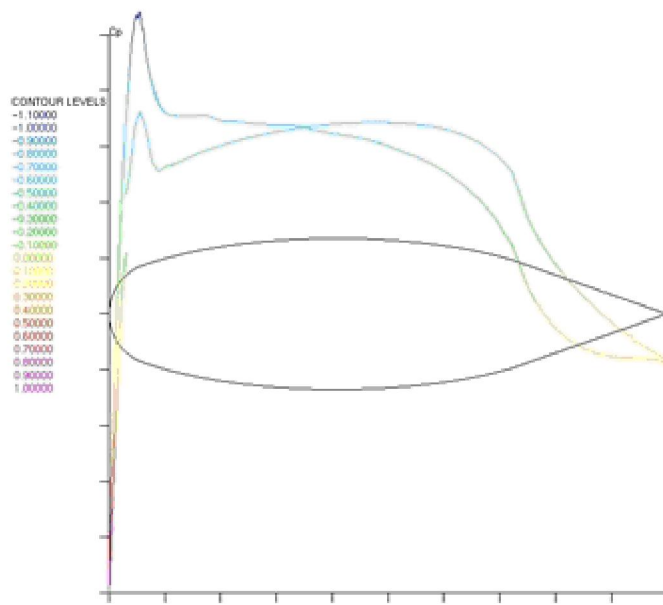


Figure 12:  $C_L$  vs.  $\alpha$  for the Ellipse with a Cusp, no trips

Figure 13 shows the streamlines at the trailing edge of the ellipse with the cusp at 2 degrees angles of attack, which reveals that as predicted the lower surface of the airfoil has attached flow and there is growth on the upper surface. Figure 14 shows a plot of  $C_p$  vs.  $x/c$  for the ellipse with the cusp. It indicates the negative lift occurs when the area under the curve of  $\Delta C_p$  near the trailing edge surpasses the area under the curve near the leading edge. Both plots illustrate that the CFD results are able to predict this behavior that is expected theoretically.



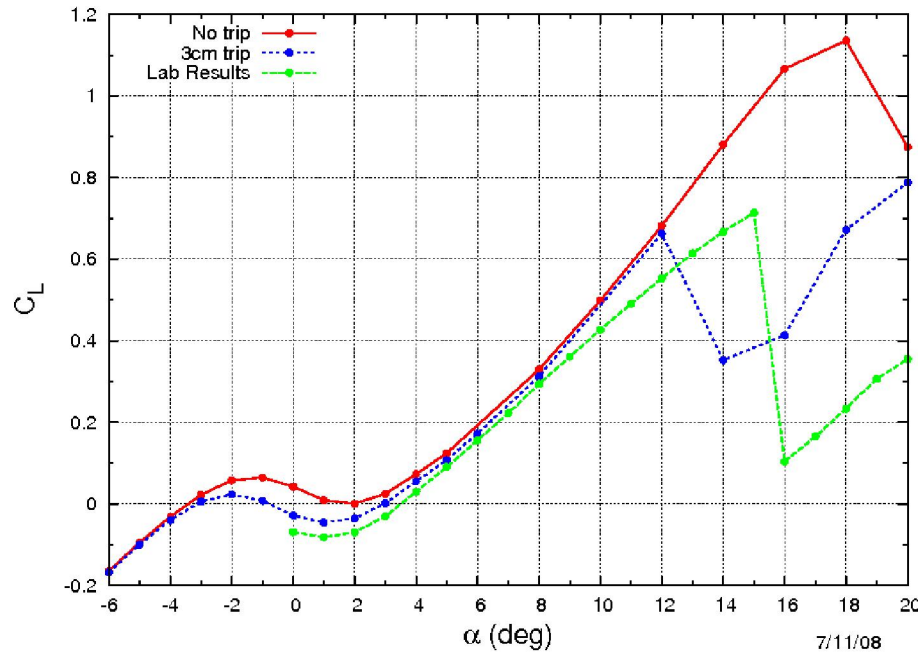
**Figure 13: Streamlines at the Trailing Edge of the Ellipse with a Cusp at 2 degrees**



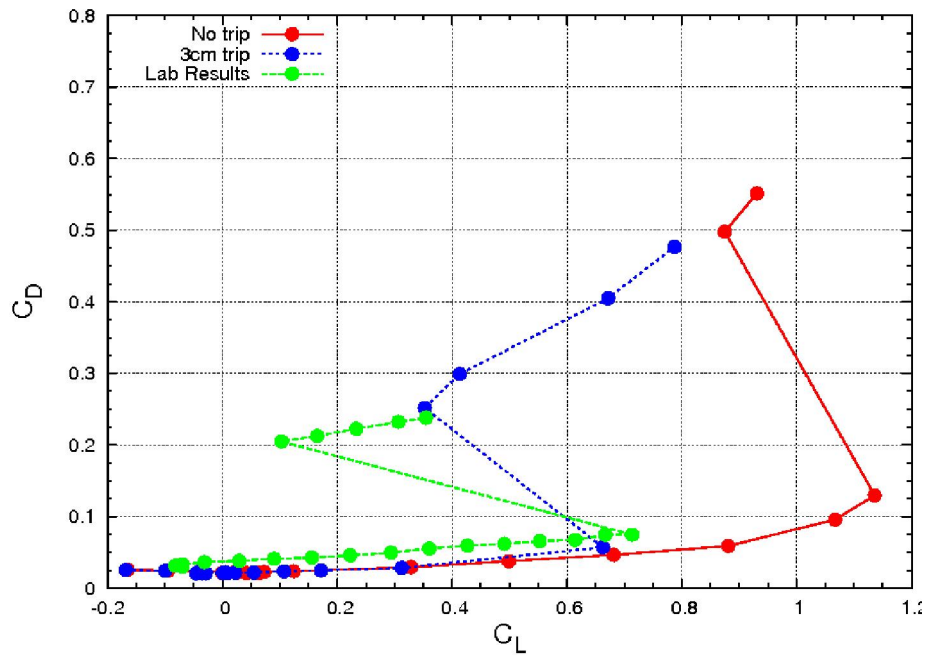
**Figure 14:  $C_p$  vs.  $x/c$  the Ellipse with a Cusp at 2 degrees**

Figure 15 shows how a trip at the leading edge causes an earlier stall of the airfoil, but does little to affect the negative lift-slope curve for small angles of attack. The figure also compares the two CFD results to the lab results. Again, it is preferable to prescribe a laminar-turbulent transition location because it predicts the stall angle of the airfoil better. In this case the ellipse laminar-transition location was prescribed at 11% ellipse chord (3cm), and so the predicted stall angle does not coincide with the lab results. Better results would be found with a

trip further downstream. However, a 3cm trip is preferable to no trip. Again in Figure 15(b), the drag coefficient is well predicted up to stall. However, after stall the lab results are not well predicted by the CFD results.



(a)



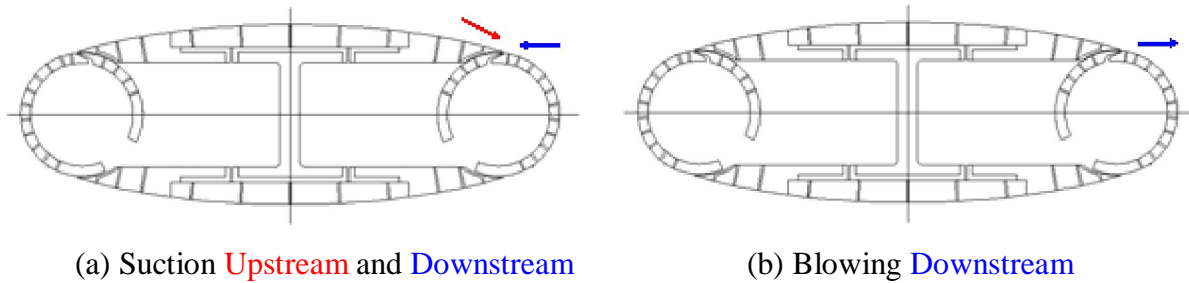
(b)

Figure 15:  $C_L$  vs.  $\alpha$  and  $C_D$  vs.  $C_L$  for the Tripped Ellipse with a Cusp

## 5.2 Active Flow Control

### 5.2.1 Steady Suction and Blowing at Trailing Edge

Next, suction and blowing were applied at the trailing edge of the ellipse. Suction and blowing were both applied by pointing the slot downstream. Also, suction was applied in two different directions by changing the orientation of the ellipse so that the slot was pointed upstream. A diagram of blowing and suction for both upstream and downstream configuration of the slot is shown in Figure 16.

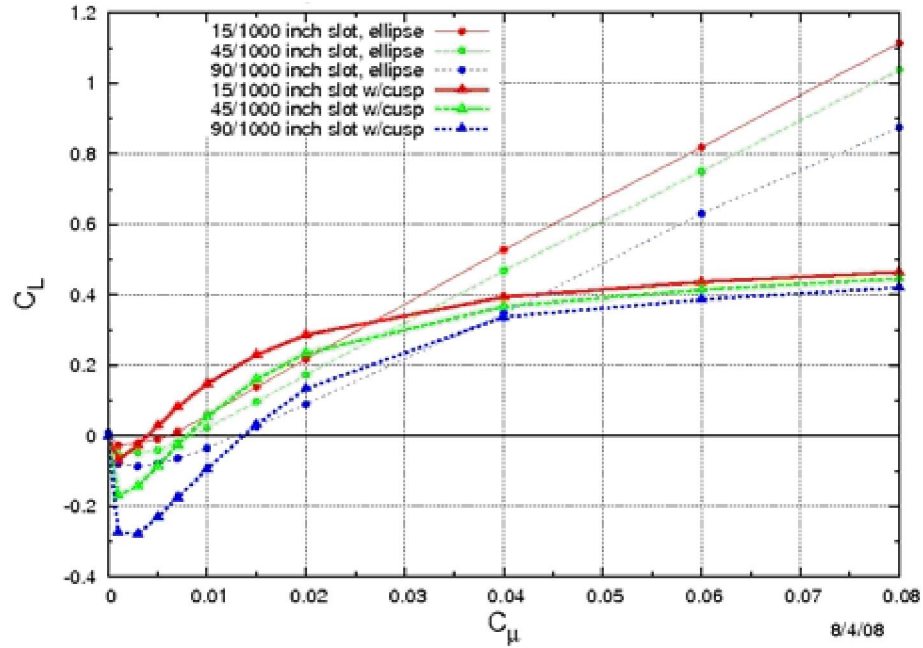
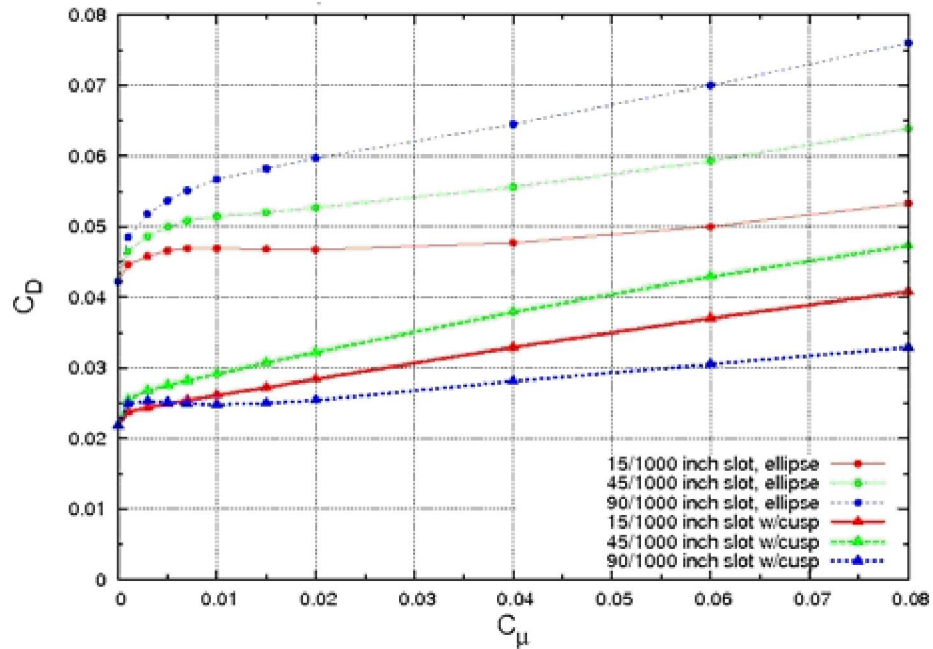


**Figure 16: A Diagram of Trailing Edge Suction and Blowing**

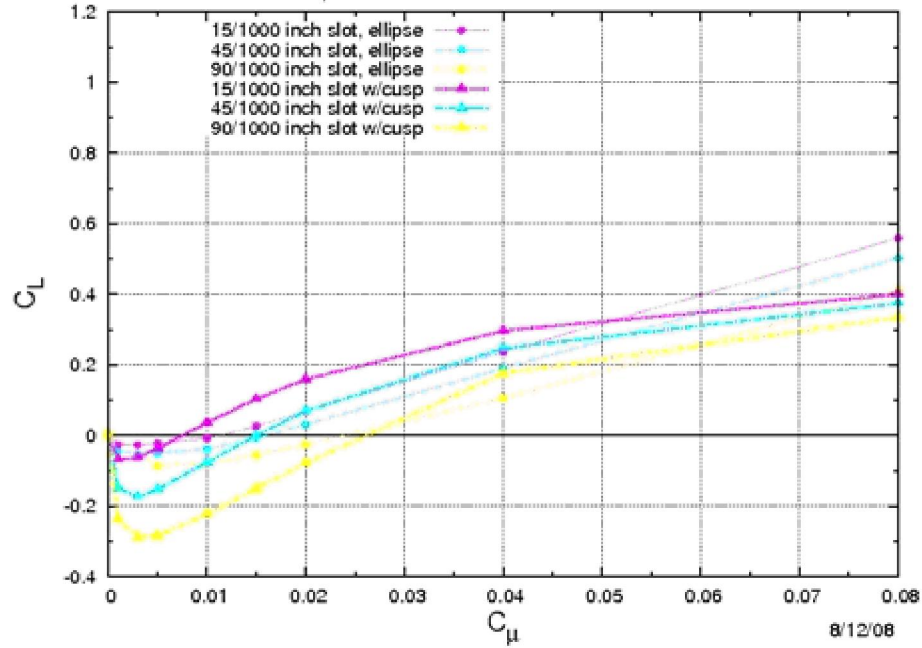
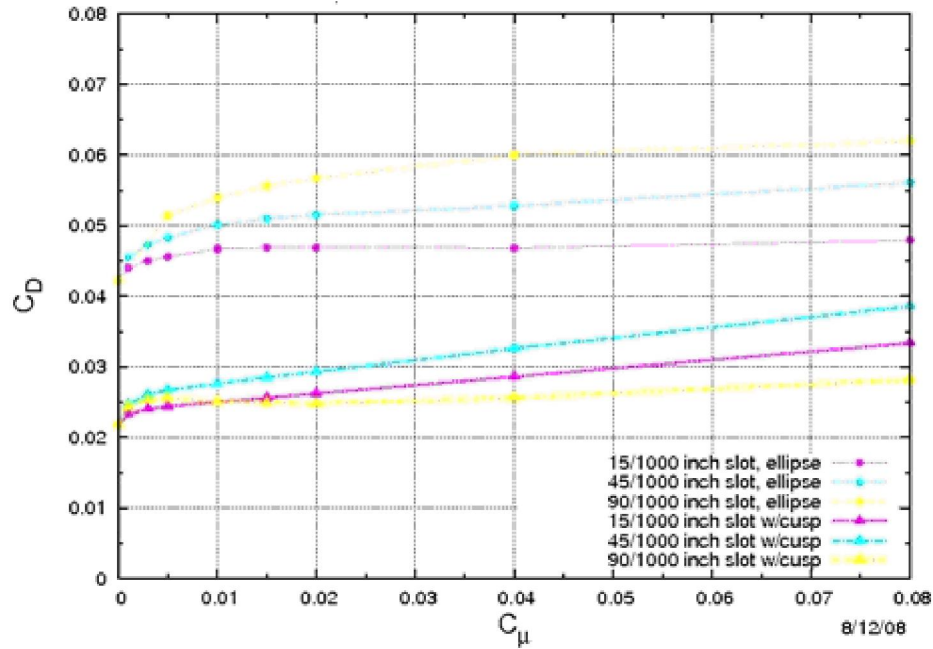
The slot width was varied from 15/1000 in. to 90/1000 in. and the value of the momentum coefficient was varied between 0% and 8%. All calculations were done at zero angle of attack. Plots were made of  $C_L$  vs.  $C_\mu$  and  $C_D$  vs.  $C_\mu$  to study how suction and blowing can best be utilized in active flow control. Figures 17, 18, and 19 show plots of  $C_L$  vs.  $C_\mu$  and  $C_D$  vs.  $C_\mu$  with varying slot widths for both the ellipse and the ellipse with a cusp. Figure 20 compares methods suction and blowing for a single value of the slot width.

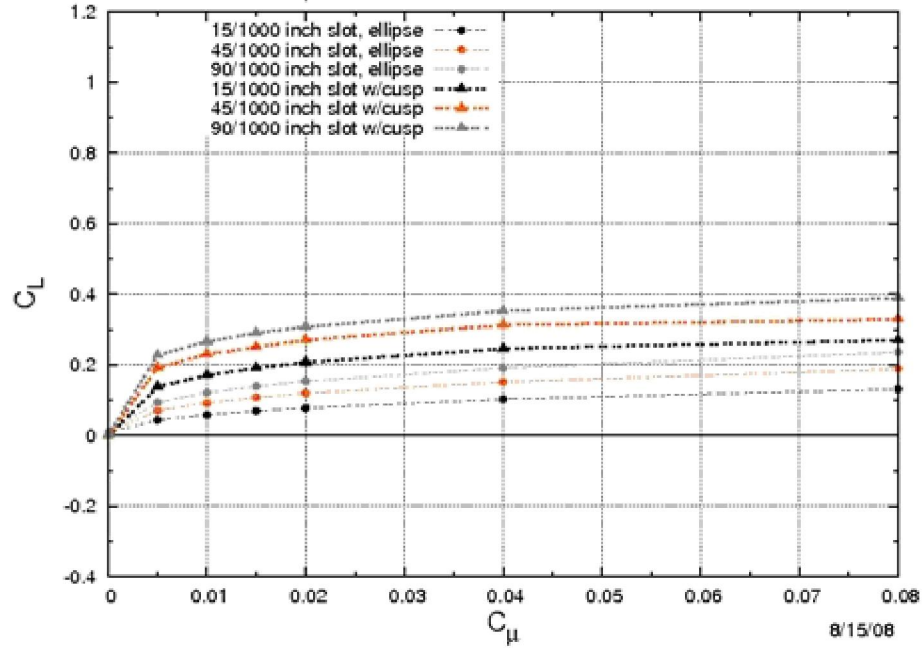
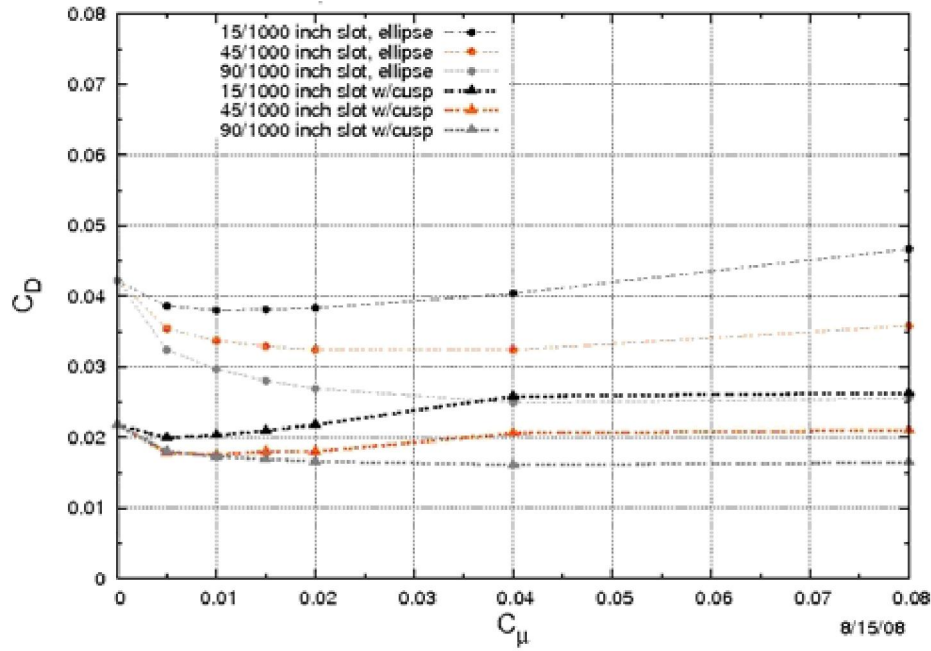
Figure 21 compares one of these results to the results obtained experimentally for the ellipse with the cusp. From this figure, it is clear that CFD predicts the same negative lift for small values of the momentum coefficient. However, the values of the lift coefficient found in the lab are considerably lower than those predicted by CFD for high momentum coefficients. The lift coefficients predicted for suction are actually closer to the lab results for steady blowing for high momentum coefficients.

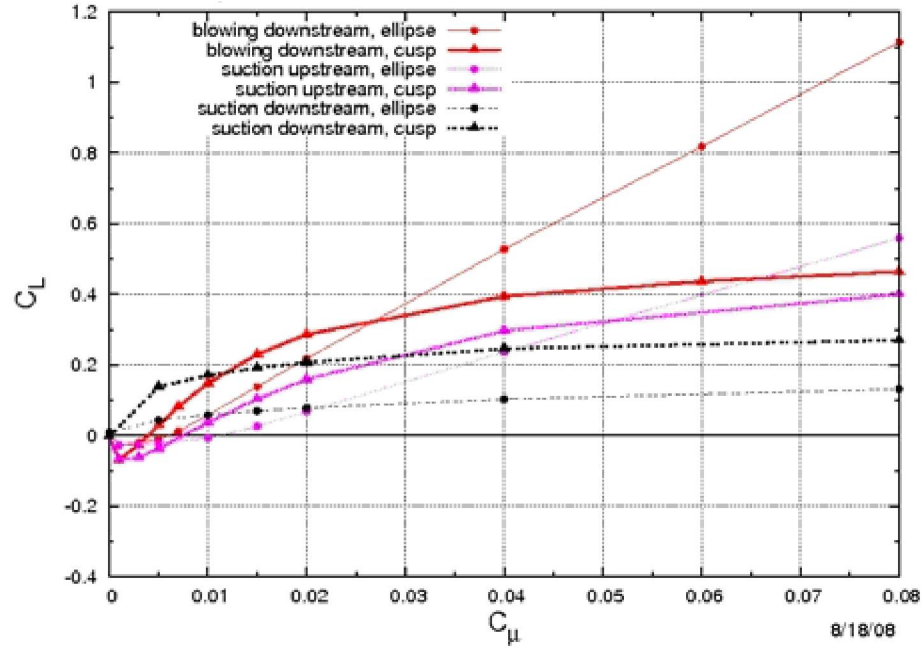


(a) Blowing Downstream  $C_L$  vs.  $C_\mu$ (b) Blowing Downstream  $C_D$  vs.  $C_\mu$ Figure 17:  $C_L$  and  $C_D$  for blowing downstream for varying slot widths and  $C_\mu$

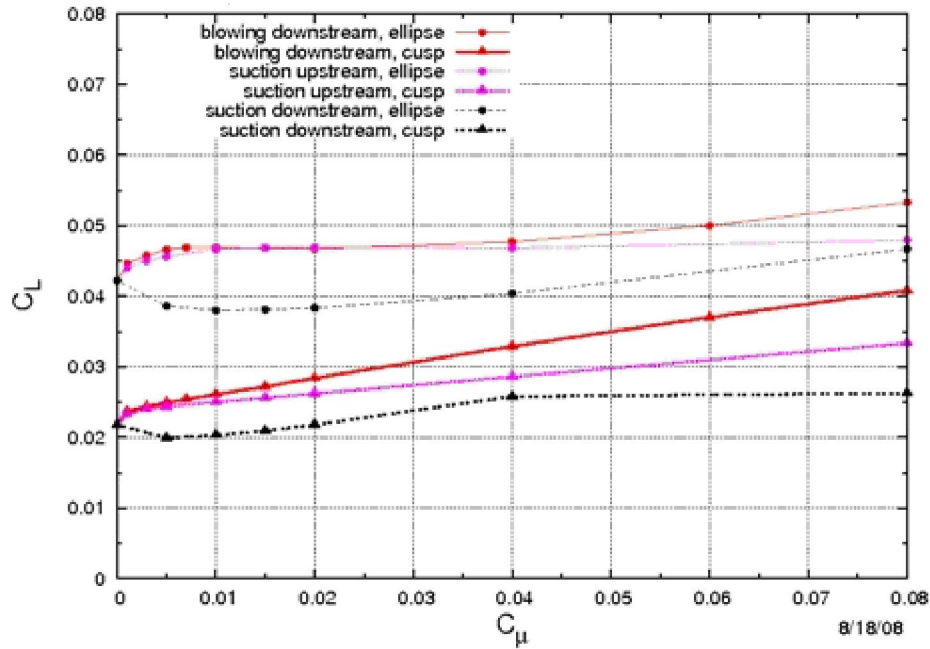


(a) Suction Upstream  $C_L$  vs.  $C_\mu$ (b) Suction Upstream  $C_D$  vs.  $C_\mu$ **Figure 18:  $C_L$  and  $C_D$  for suction upstream for varying slot widths and  $C_\mu$**

(a) Suction Downstream  $C_L$  vs.  $C_\mu$ (b) Suction Downstream  $C_D$  vs.  $C_\mu$ Figure 19:  $C_L$  and  $C_D$  for suction downstream for varying slot widths and  $C_\mu$

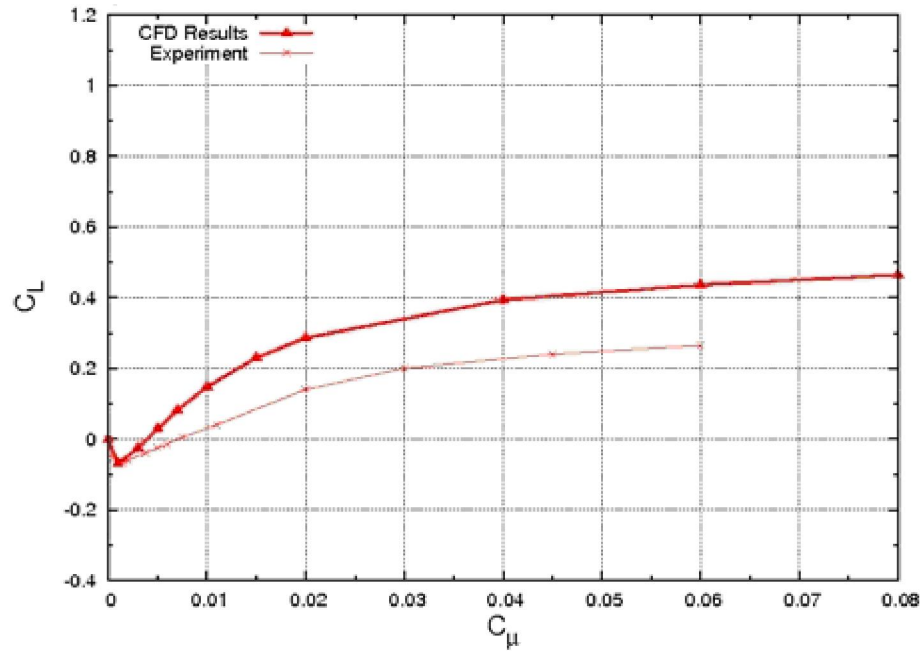


(a) Slot width of 15/1000 inch,  $C_L$  vs.  $C_\mu$

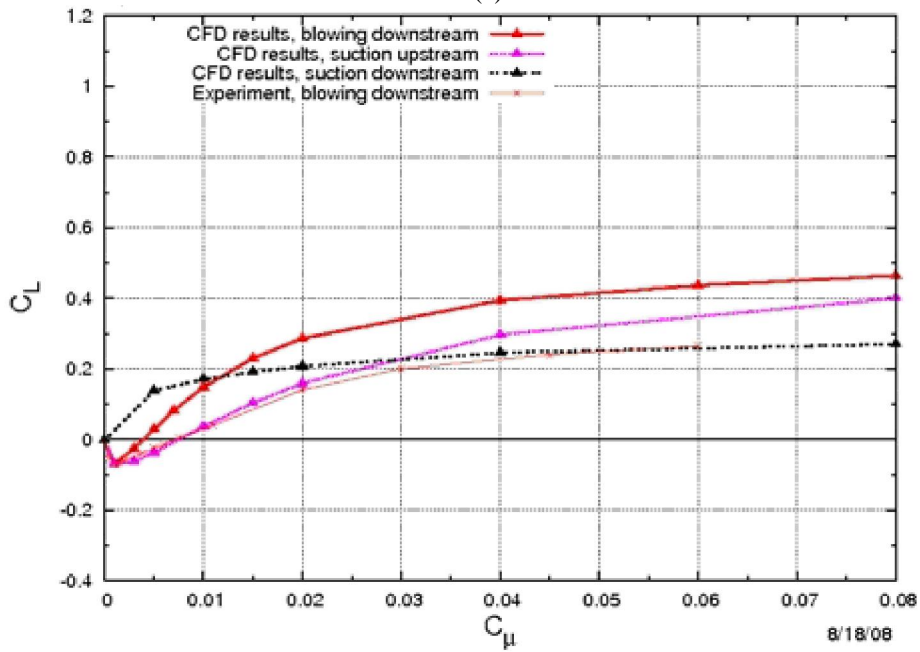


(b) Slot width of 15/1000 inch,  $C_D$  vs.  $C_\mu$

Figure 20:  $C_L$  vs.  $C_\mu$  and  $C_D$  vs.  $C_\mu$  for TE suction and blowing at  $h = 15/1000$  inch



(a)



(b)

Figure 21:  $C_L$  vs.  $C_\mu$  for the Ellipse with Cusp, CFD and Lab Results, 15/1000 inch slot

Figure 22 compares the CFD results to some of the experimental results for the ellipse. In this case, the CFD results underestimate the lift coefficients that are obtained in the lab both for blowing downstream and suction upstream. However, CFD results again are accurately able to predict the shape of the curve. Also, they accurately predict the negative lift coefficient for small

values of the momentum coefficient for blowing downstream.

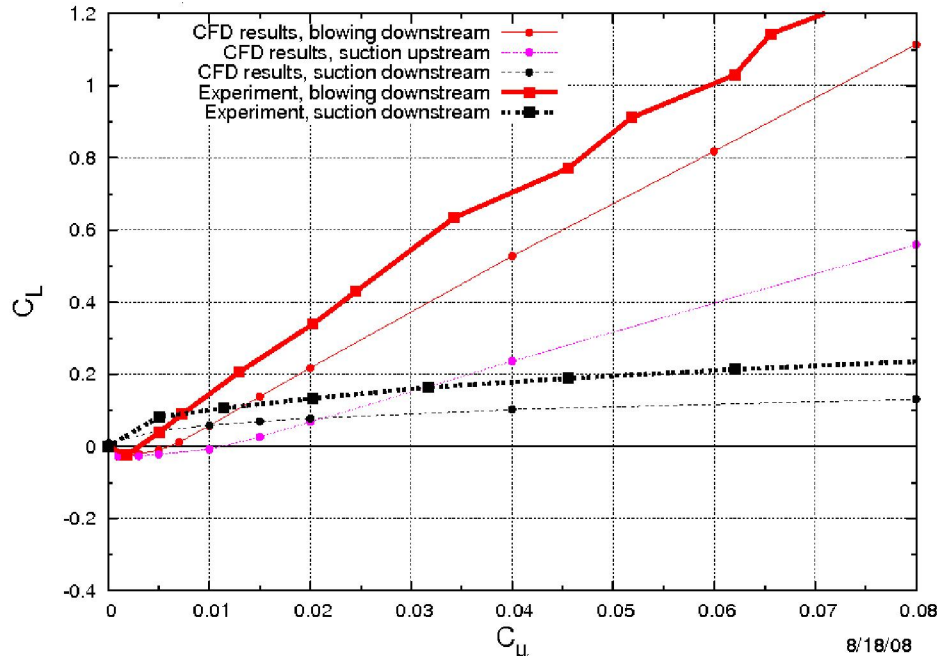


Figure 22:  $C_L$  vs.  $C_\mu$  for the Ellipse, CFD and Lab Results, 15/1000 inch slot

Figure 23 shows the velocity contours behind the ellipse when steady blowing is applied at  $C_\mu = 8\%$ . This figure shows how blowing at high momentum coefficients alters the behavior near the trailing edge and results in very high lift coefficients even at zero angle of attack. In order to see why there is a negative lift for the ellipse with the cusp for trailing edge blowing, Figure 24(a) was made to show the stream function behind the ellipse with the cusp. It is very similar to the stream function shown in Figure 13 for the ellipse with a cusp at low angles of attack. So, it is concluded that the negative lift slope for low momentum coefficients occurs for a similar reason as it did for low angles of attack. It is a result of the high thickness of the airfoil coupled with a relatively high trailing edge cusp angle.

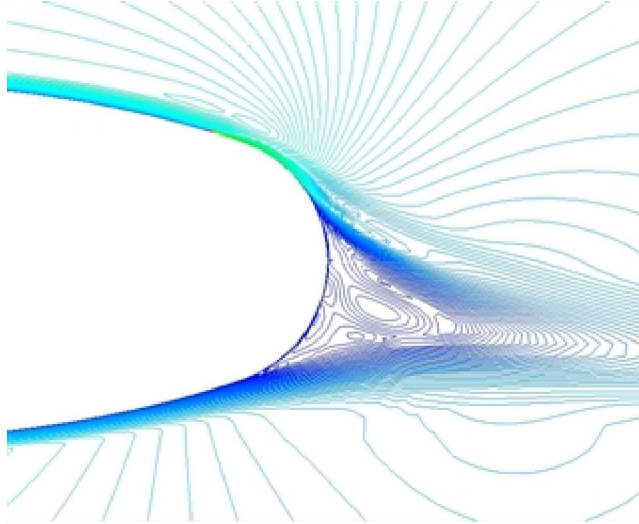
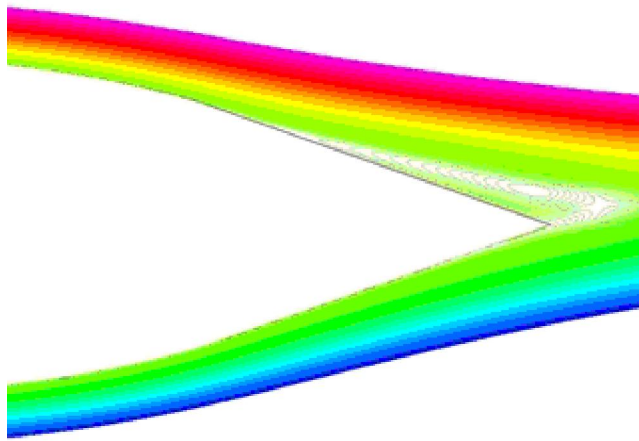
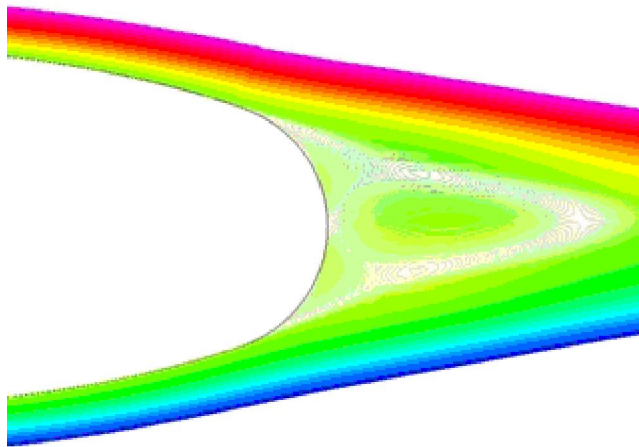


Figure 23: Velocity contours for the ellipse with steady blowing,  $C_\mu = 8\%$



(a) Ellipse with Cusp

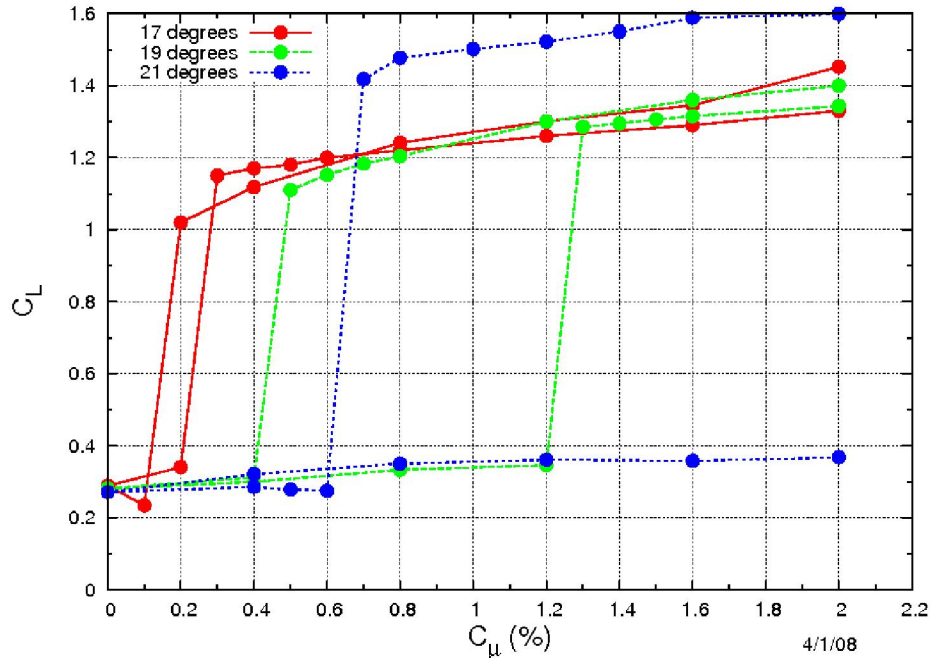


(b) Ellipse

Figure 24: Stream function for  $C_\mu = 0.1\%$  and  $h = 90/1000$  in

### 5.2.2 Steady Suction at Leading Edge

When steady suction is applied to the leading edge of the elliptical airfoil, stall is significantly delayed from the baseline case. Also, the lift is significantly increased. It is important to study how the airfoil will stall in this case if steady suction is turned off, or gradually decreased from some starting value of the momentum coefficient  $C_\mu$ . This effect, similar to the more well known effect of dynamic lift stall and will result in a hysteresis loop and is especially important in the designs of helicopters as it may lead to stall flutter. The hysteresis was modeled in CFL3D by using the Suction/Blowing boundary condition and applying a momentum coefficient of 2% at some angle of attack (varied from 17 to 21 degrees). By restarting the solution from the 2%  $C_\mu$  case at lower values of  $C_\mu$ , plots of the upper hysteresis loop were generated. Also, by restarting the solution from the 0%  $C_\mu$  case at higher values of  $C_\mu$ , plots of the lower hysteresis loop were generated and are shown in Figure 25.



(a)



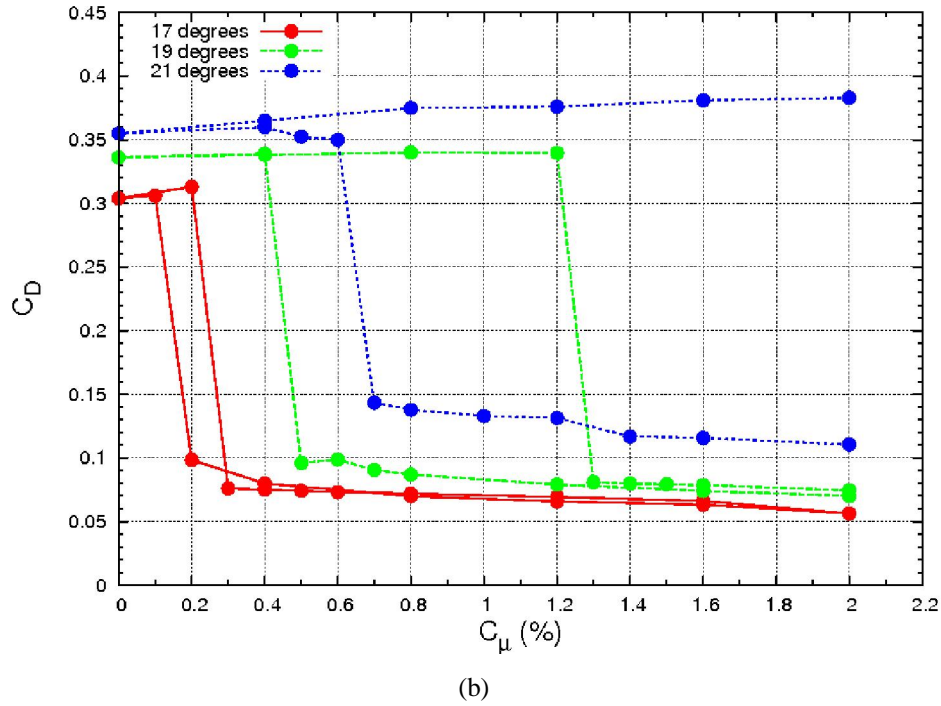
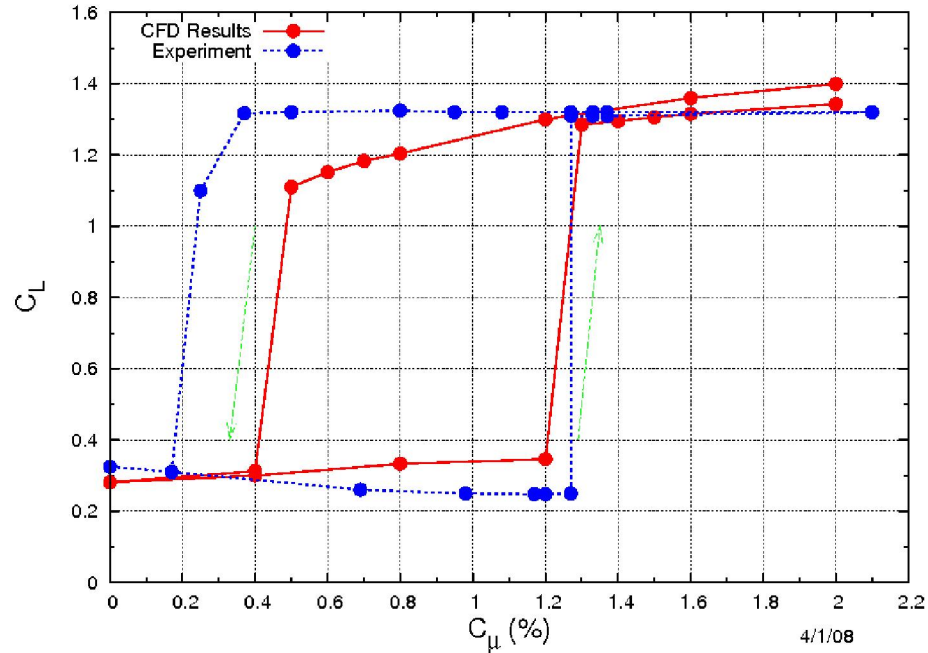


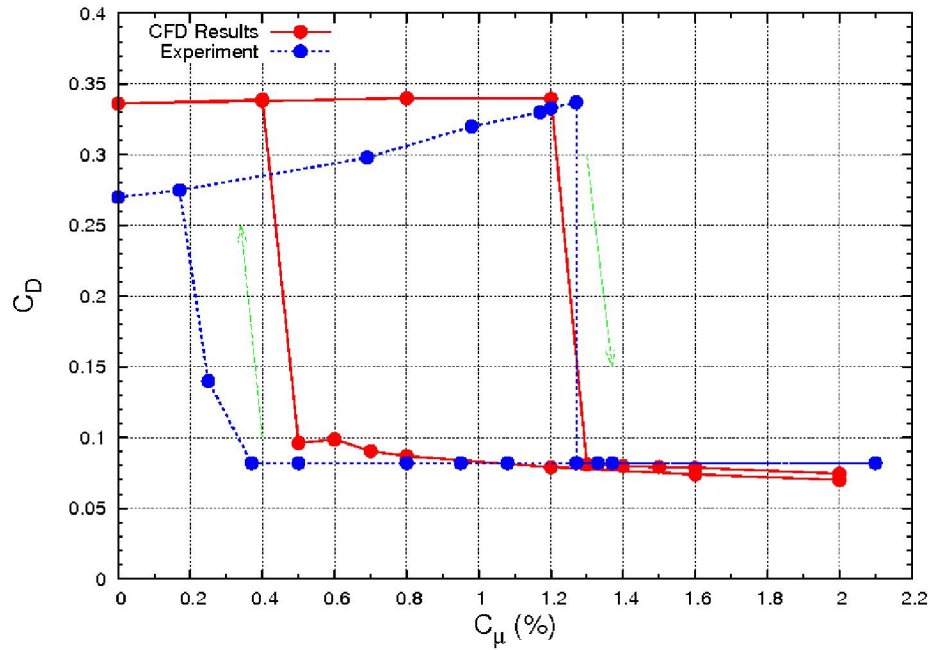
**Figure 25: Steady Suction Hysteresis Loop at 17, 19, and 21 degrees,  $h/R = 1.2\%$**

CFD results are compared with results obtained experimentally for this airfoil. They are in good agreement as shown in Figure 26. Both hysteresis loops are run at the same angle of attack of 19 degrees. Both recover from stall at nearly the same value of  $C_\mu$  (1.2%). However, the value of  $C_\mu$  that causes the ellipse to stall is slightly different. Also, in the experiments it was seen that the lift coefficient remains stable at  $C_\mu$  is decreased. However, the CFD results did not predict this effect. Rather, CFD predicts a gradual decline in  $C_L$  until stall occurs.





(a)

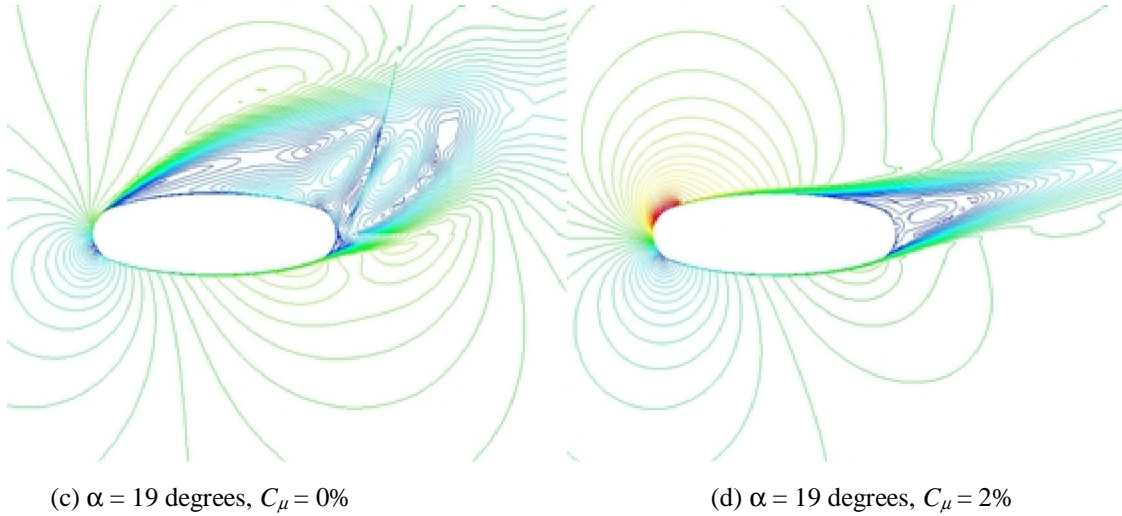


(b)

**Figure 26: Steady Suction Hysteresis Loop at 19 degrees,  $h/R = 1.2\%$**

Next, velocity contours (Figure 27) were made of the ellipse with leading edge suction to show how at a given angle of attack (19 degrees) the tripped ellipse may be stalled. However, after applying steady suction at the leading edge the ellipse will recover from the stall and the

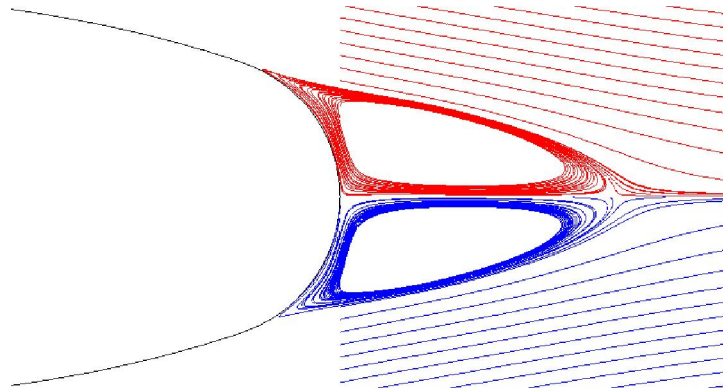
flow will reattach. As in the earlier velocity contour plots, the red lines represent lines of constant high velocity while the blue lines represent low velocity.



**Figure 27: Velocity contours for  $C_\mu = 0\%$  and  $C_\mu = 2\%$**

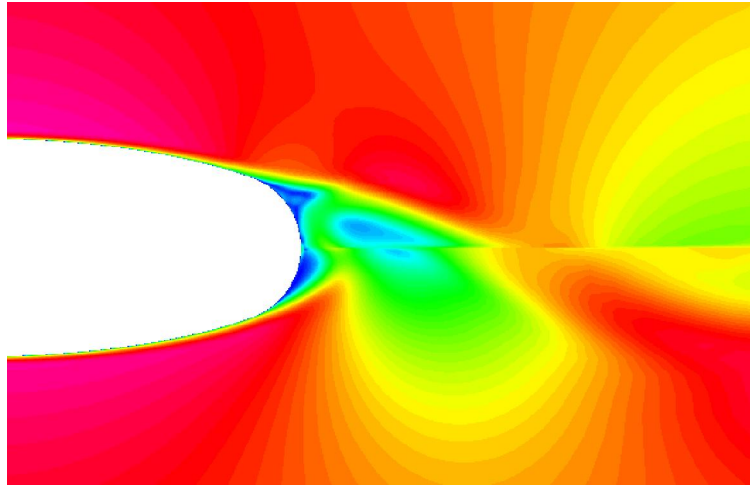
### 5.3 Time Dependent Behavior Study

The ellipse was run at zero angle of attack. It was expected that the solution would be oscillatory due to the blunt trailing edge, but the time accurate computation converged to a steady solution. Particle traces were taken (Figure 28), revealing a flow field characteristic of very low Reynolds numbers. This computation employed a time step  $dt = 0.01$  with the number of sub-iterations  $ncyc = 8$ .

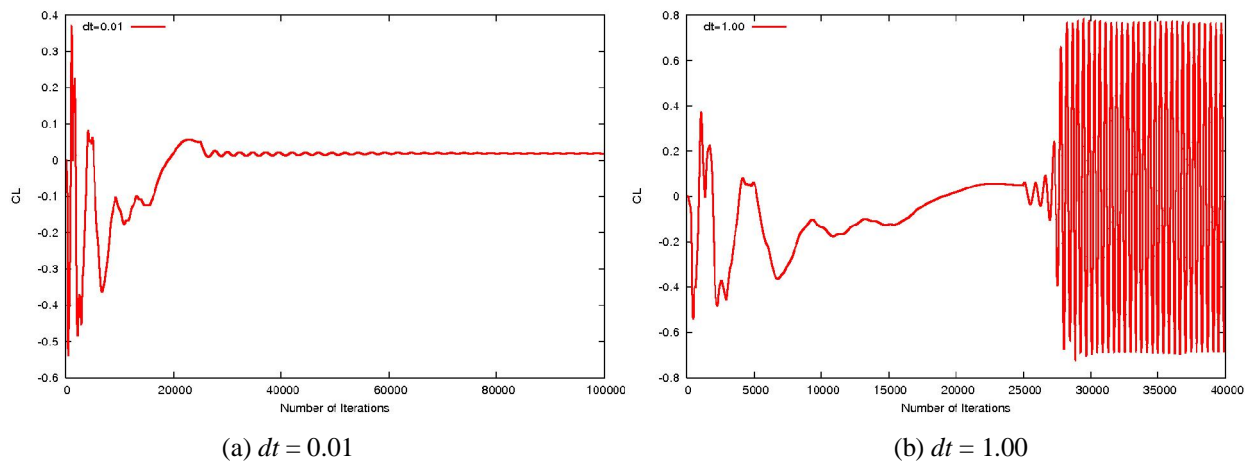


**Figure 28: Particle traces in the wake behind the ellipse,  $dt = 0.01$**

It was guessed that the value of the time step was too low. So,  $dt$  was increased to 1.00. An oscillatory solution was observed, but it was not a good solution. The residuals were high and the oscillations in the lift coefficient were too large. Pictures of the flow field were taken showing that the solution was not resolved between the boundaries of the grids in the wake (Figure 29). Also, plots of  $C_L$  vs. Number of Iterations were made to observe the difference in the solutions for the two values of  $dt$  (Figure 30).



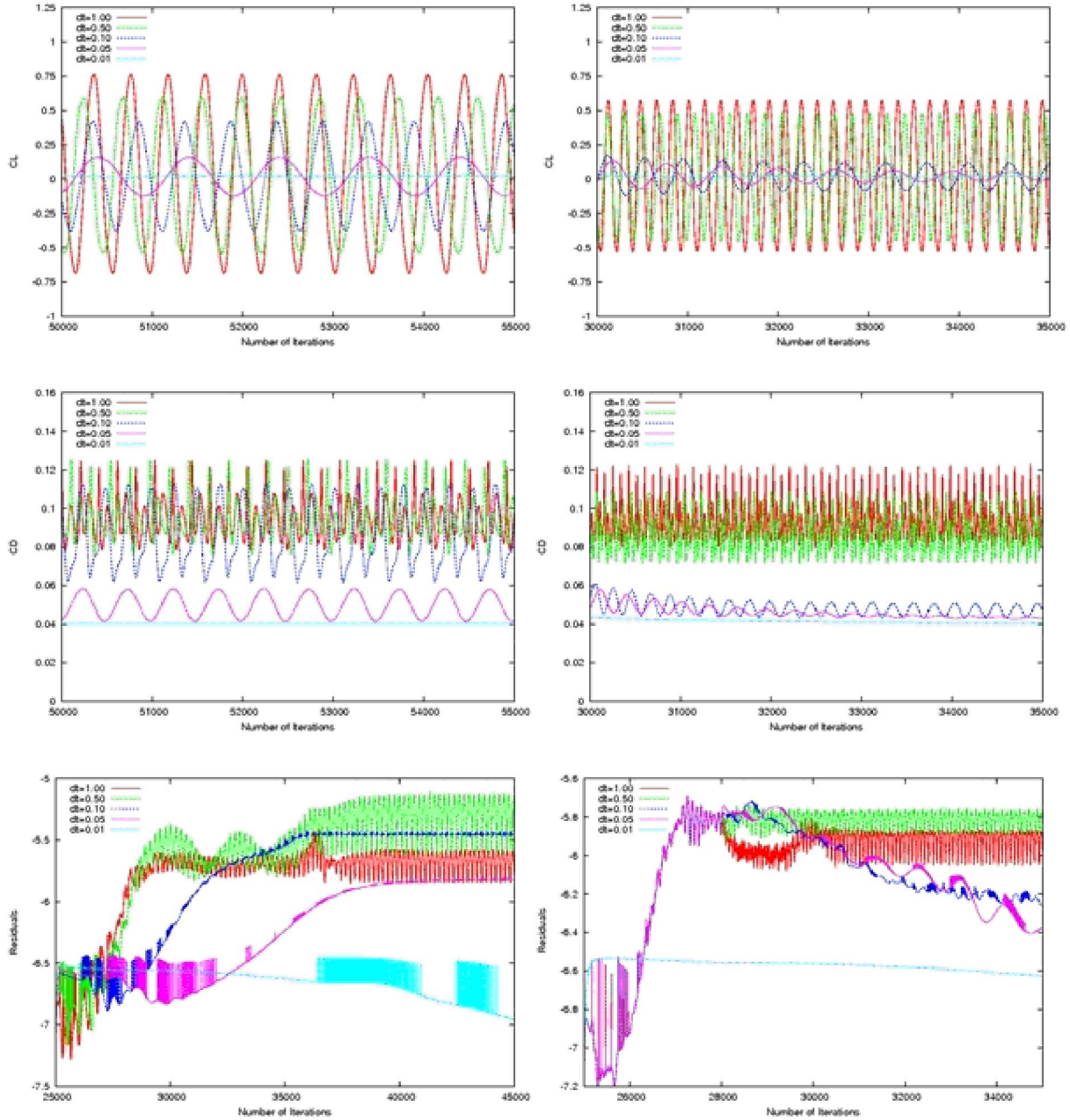
**Figure 29: Velocity magnitude contours for a solution not resolved at grid boundaries,  $dt = 1.00$**



**Figure 30:  $C_L$  vs. Number of iterations, zero AOA, ncyc= 12, for two values of  $dt$**

### 5.3.1 Varying Time Steps

The time step was then varied between 1.00 and 0.01 to see if there was a region where the solution seemed viable. It was found that the frequency and amplitude of the unsteady solution varied widely with the time step (Figure 31a). As the time step was decreased, the amplitude of oscillations in  $C_L$  would decrease, and the value of  $C_D$  and it's amplitude of oscillations would also decrease (Figure 31b). To see if this occurred at other values for the number of sub-iterations,  $ncyc$ , solutions for a higher number of  $ncyc = 30$  were run.

(a)  $ncyc = 12$ (b)  $ncyc = 30$ Figure 31:  $C_L$ ,  $C_D$ , and Residuals vs. Number of Iterations, varied time steps

### 5.3.2 Varying the Number of Subiterations

It was found that the value of  $ncyc$  also affected the solution. To analyze these effects,  $dt$  was held constant while varying the number of cycles from 6 to 42. (Figure 32) It was found that increasing number of cycles had nearly the same effect as decreasing the time step. This may be because increasing  $ncyc$  and decreasing  $dt$  both increase the number of computations performed per unit time (or pseudo time). Namely, decreasing  $dt$  will decrease the time step used in computations. And increasing  $ncyc$  will decrease the psuedo time step  $d\tau$  used to compute the subiterations.

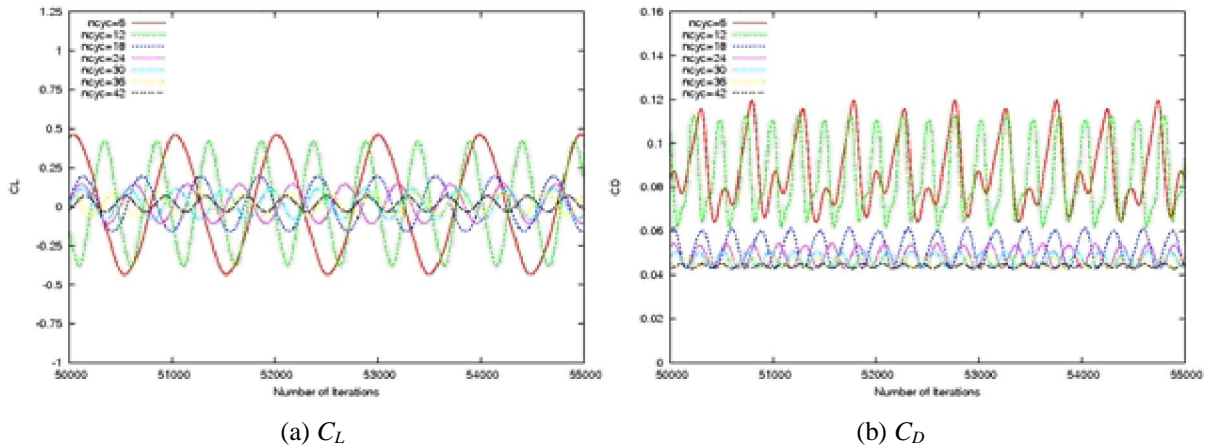


Figure 32:  $C_L$  and  $C_D$  vs. number of iterations,  $dt = 0.10$ , varying  $ncyc$

### 5.3.3 Issues with the Residuals

As  $ncyc$  increased (or as  $dt$  was decreased) and the solution converged to a steady solution, it was observed that the residuals would decrease. (Figure 33a) However, as the residuals decreased there were frequent jumps in value of the residuals. (Figure 33b) These jumps increase in magnitude as the solution becomes steadier. The heavy dependence of the solution on  $dt$  and  $ncyc$ , along with the jumps in the residuals for converged solutions indicate that the numerical model is not converging to a good solution.



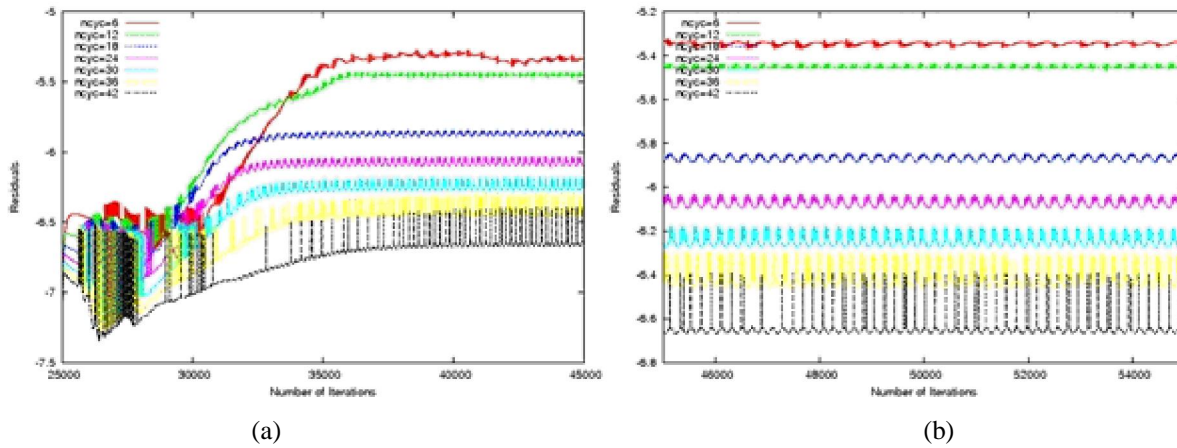


Figure 33: Residuals vs. number of iterations,  $dt = 0.10$ , varying  $ncyc$

### 5.3.4 Issues for a Wide Variety of Physical Parameters

At this point, the same case was run while some CFD parameters were changed in order to determine the cause of the strange solutions. First, the Mach number was increased and the low Mach number preconditioning was turned off. It was thought that perhaps the strange solutions could be a result of some issues with low Mach number preconditioning. (Figure 34) Next, the code was run with “full” Navier-Stokes. Because CFL3D is a thin-layer solver, the viscous derivatives are included in selected coordinate directions, but cross-derivative terms are ignored. However, the cross-derivatives are included with “full” Navier-Stokes by setting a keyword `ifullns=1` and selecting the streamwise (j) and normal (k) directions. (Figure 35) Also, the blocks were removed and the code was run in series rather than parallel to test if the solutions were poor as a result of an incorrect setup of the parallel code or input files. (Figure 36) However, in all cases the strange solutions and oscillations continued.

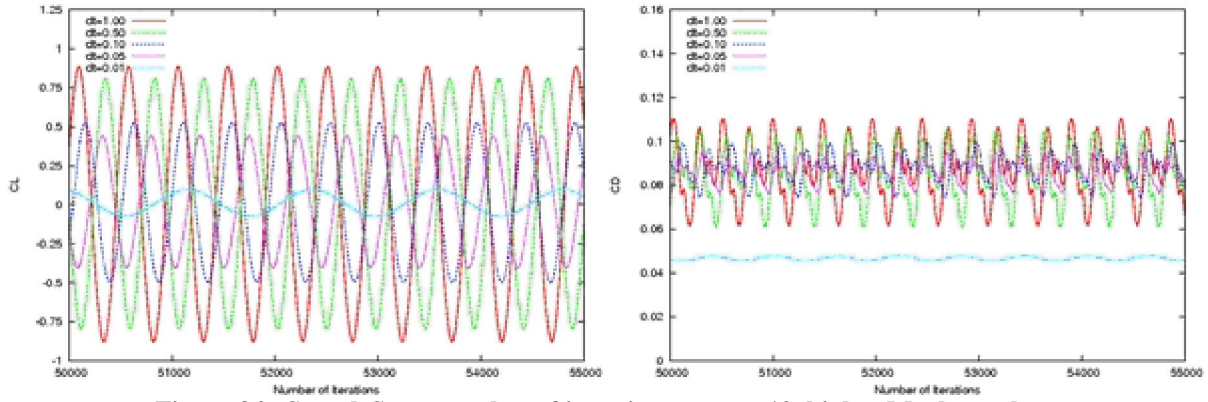


Figure 34:  $C_L$  and  $C_D$  vs. number of iterations, ncyc = 12, higher Mach number

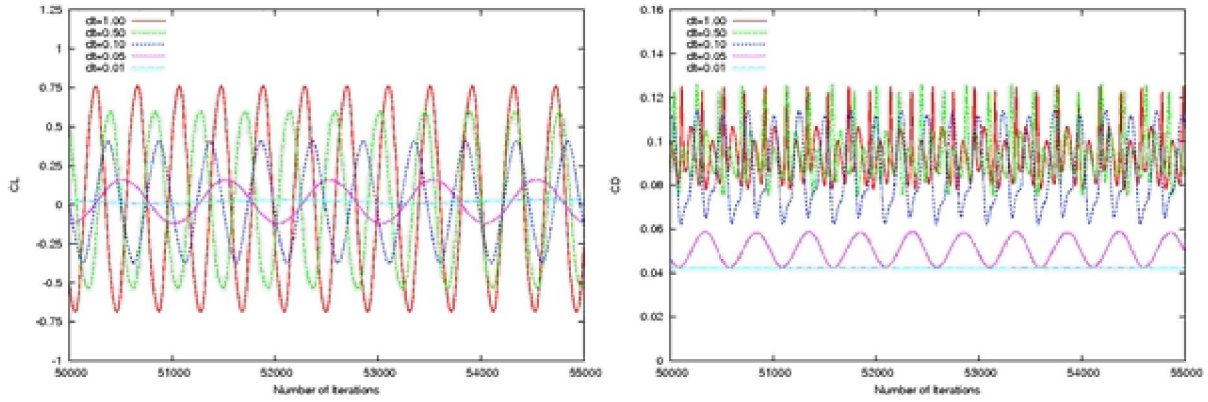


Figure 35:  $C_L$  and  $C_D$  vs. number of iterations, ncyc = 12, full Navier Stokes

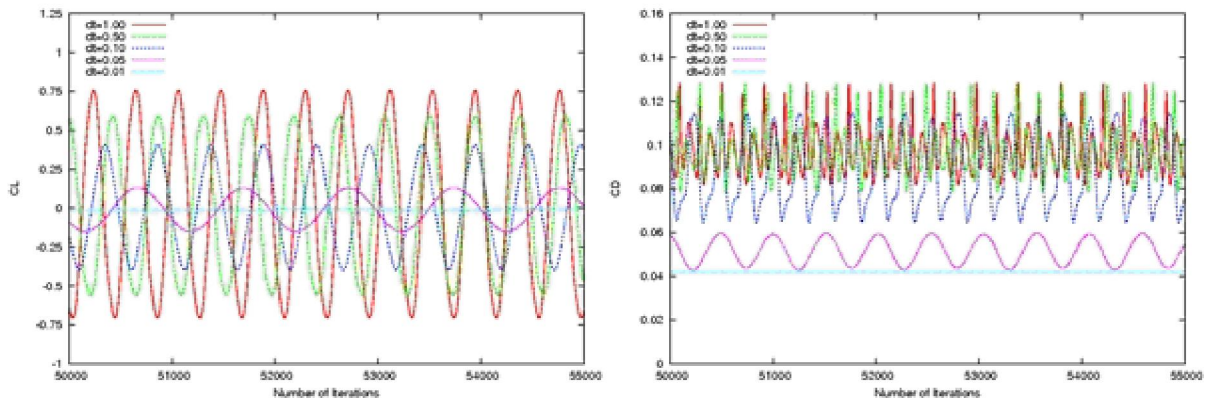


Figure 36:  $C_L$  and  $C_D$  vs. number of iterations, ncyc = 12, series computation

### 5.3.5 Baldwin-Lomax Solution

It was thought that perhaps the Spalart-Allmaras turbulence model was the source of the problem. Another turbulence model known to be robust in CFL3D is Baldwin-Lomax with Degani-Schiff modification (ivisc=3). It was employed in the normal (k) direction. The results were surprisingly good. As  $dt$  and  $ncyc$  varied, the frequency and amplitude of oscillations remained the same. At high values of  $dt$  the value of  $C_D$  was oscillating too much, but for such a high time step there are not enough computations per unit time to generate a good solution. For  $dt < 0.10$  the solution looked very good (Figure 37). The residuals were also within a reasonable range of values. (Figure 38) The only issue observed was that the Strouhal number for these solutions was higher than expected.

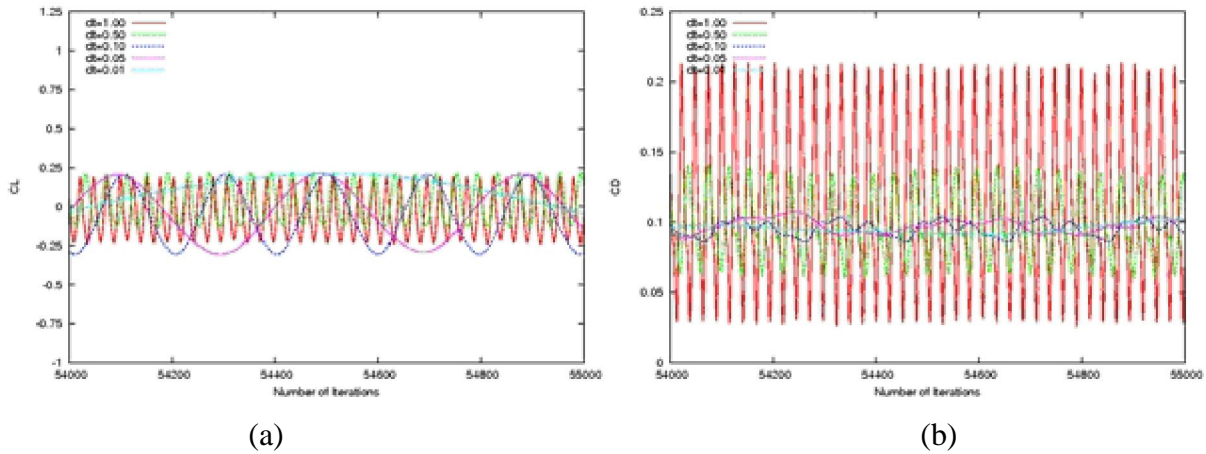


Figure 37:  $C_L$  and  $C_D$  vs. number of iterations,  $ncyc = 12$ , Baldwin-Lomax model

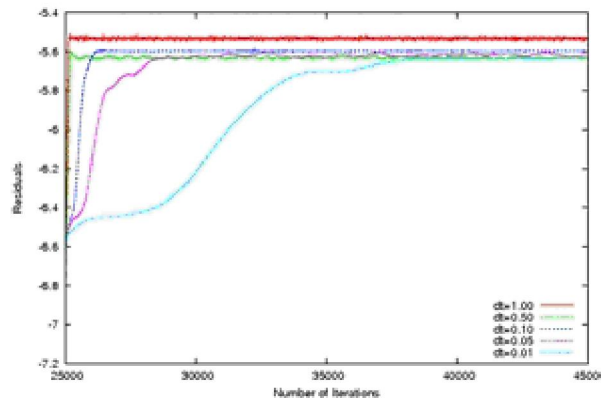
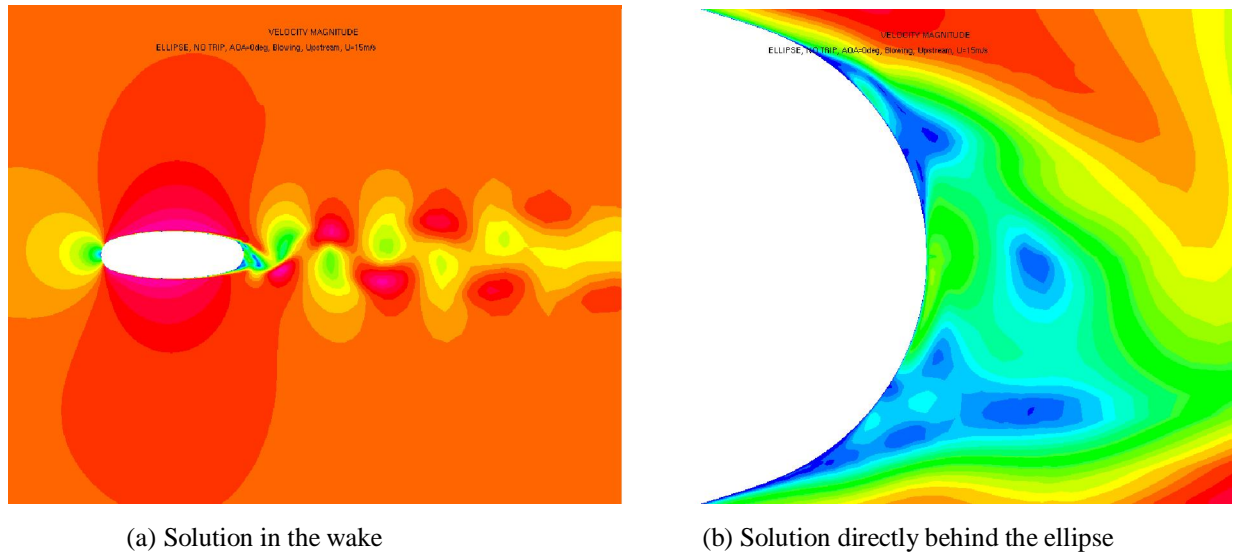


Figure 38: Residuals vs. number of iterations,  $ncyc = 12$ , Baldwin-Lomax model



Next, in order to see the behavior of the Baldwin-Lomax solution, contour plots of the velocity magnitude were made showing the characteristics of the flow directly behind the ellipse and in the wake (Figure 39). The solution behaved as expected. Physically, the behavior of the flow behind the blunt trailing edge should be similar to the behavior behind a circular cylinder. The ellipse, like the cylinder, sheds vortices alternately behind the upper and lower surfaces and these vortices propagate into the wake.



**Figure 39: Velocity contours at a given time step for the Baldwin-Lomax turbulence model**

Next, for the Baldwin-Lomax turbulence model the angle of attack was varied from 0 to 20 degrees and plots of the velocity and pressure contours were made (Figures 40 and 41). As in the earlier plots for the Spalart-Allmaras model, the red lines indicate low velocities while the blue lines indicate high velocities. It is clear from these plots that there is a wide unsteady wake for all angles attack, whereas in Figures 7 and 8 it was seen that the flow was steady for all these cases. So, many of the previous calculations (the trip study and active flow control studies) were done using the steady solution computed with the Spalart-Allmaras model.

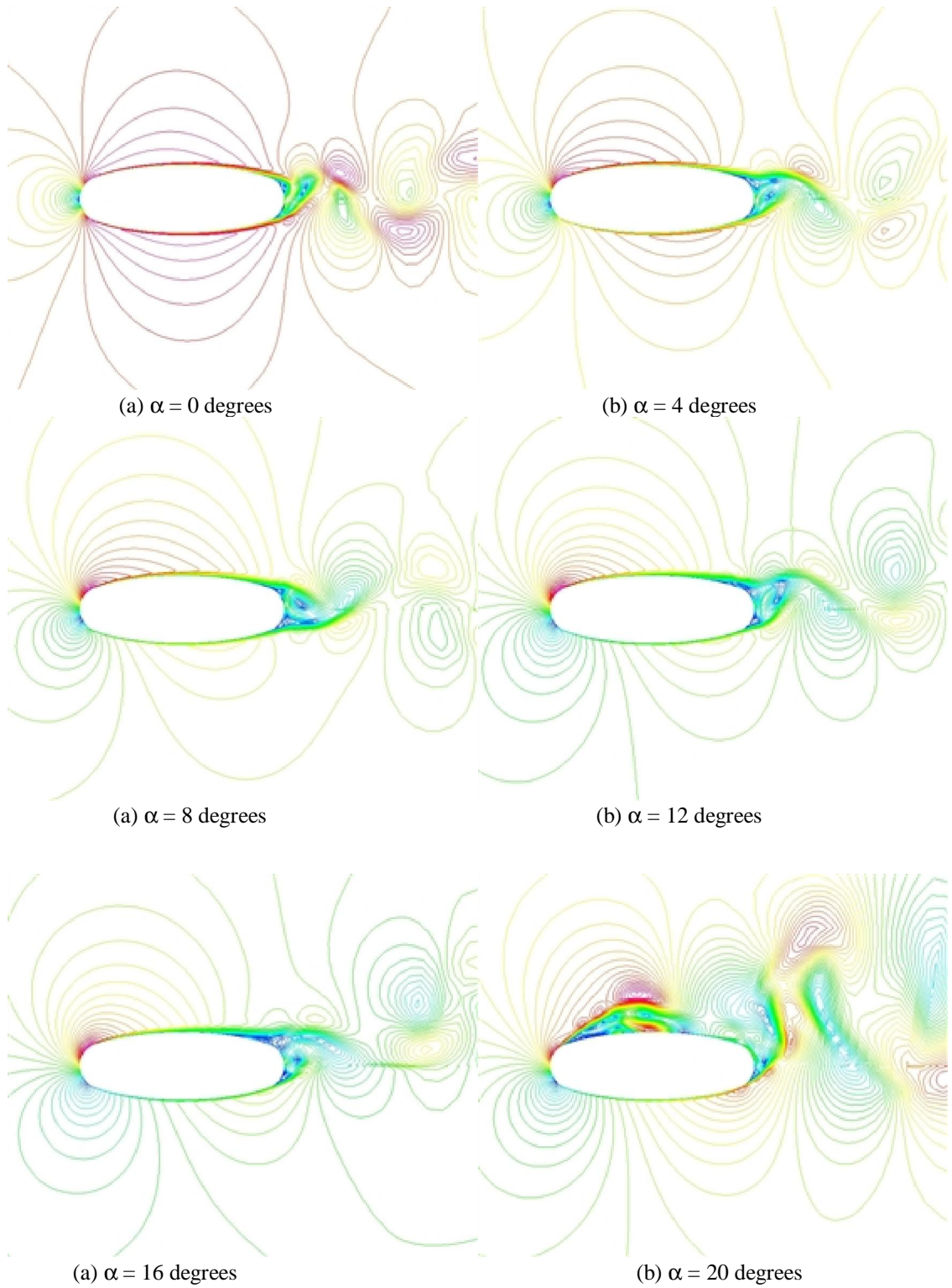


**Figure 40: Velocity contours for varying angles of attack for the Baldwin-Lomax model**

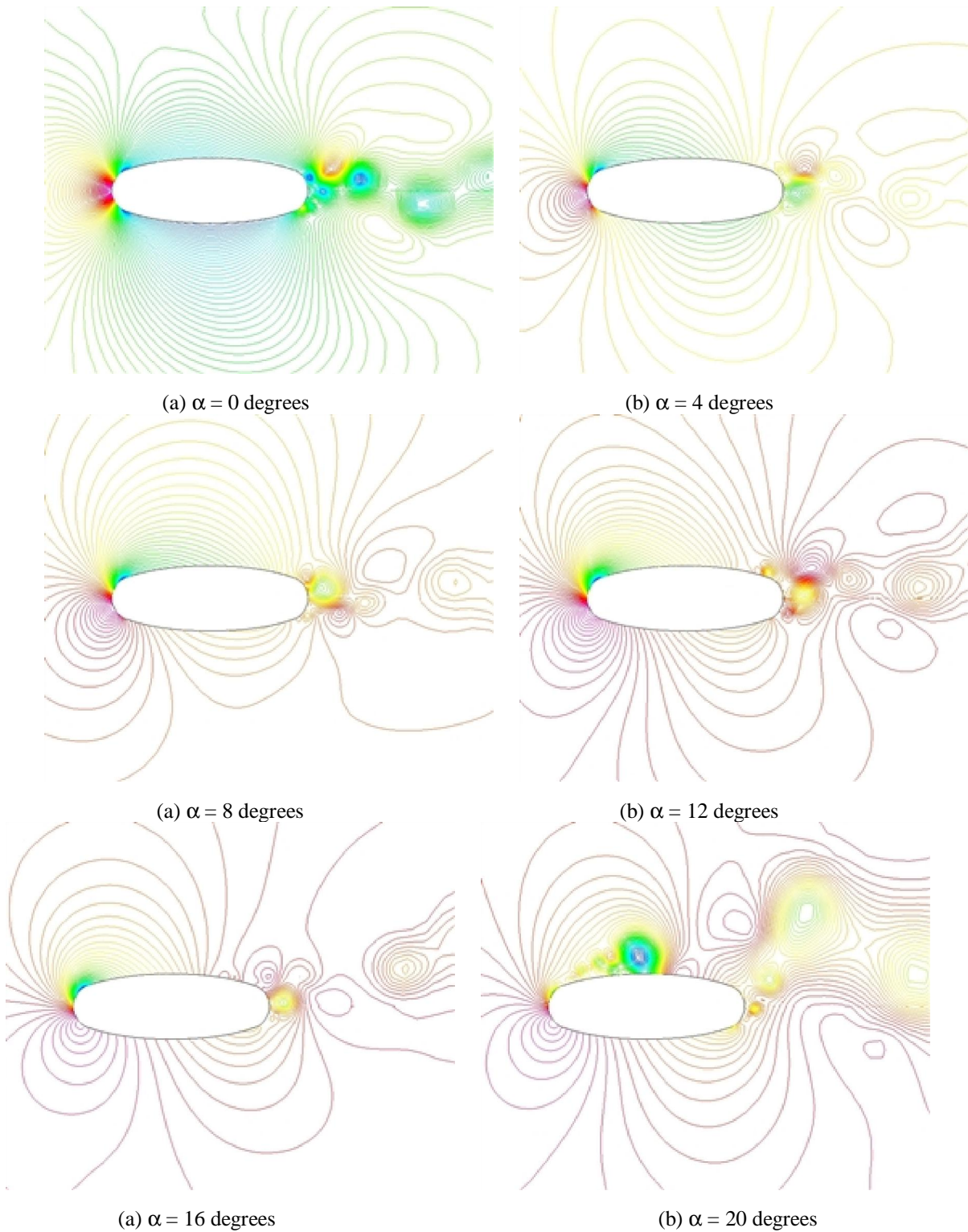


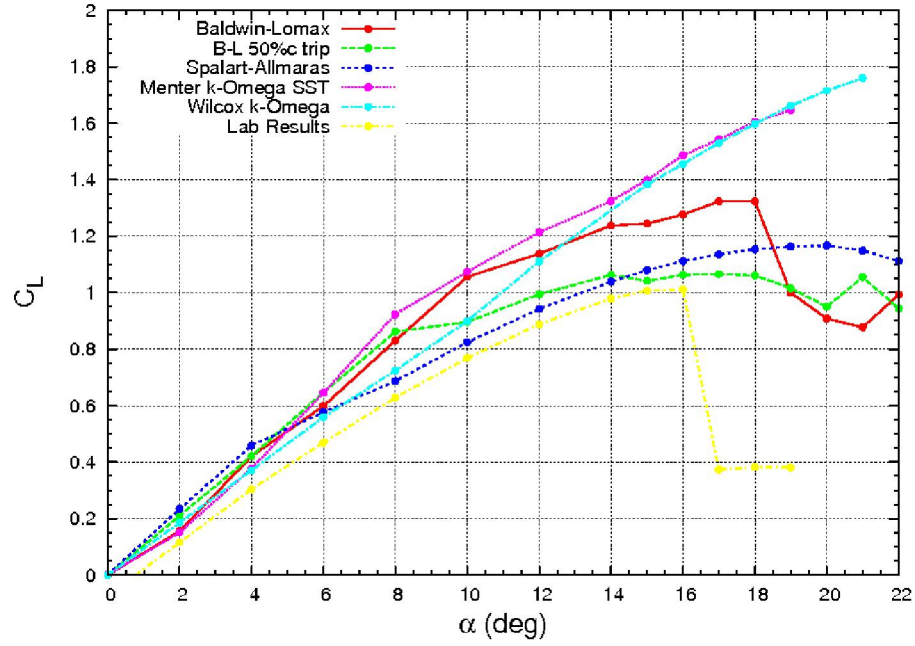
**Figure 41: Pressure contours for varying angles of attack for the Baldwin-Lomax model**

It was determined that the Spalart-Allmaras model was causing the strange solutions, and that the Baldwin-Lomax turbulence model computed a far more convincing unsteady solution. But it was not apparent why this is so, or why the Baldwin-Lomax turbulence model had no apparent issues under the same conditions. It is expected that there will be slight differences between these two turbulence models. But what is unexpected is the tendency for the Spalart-Allmaras model to converge to a steady solution, and for its solution to depend so heavily on the time step constant and the number of subiterations.

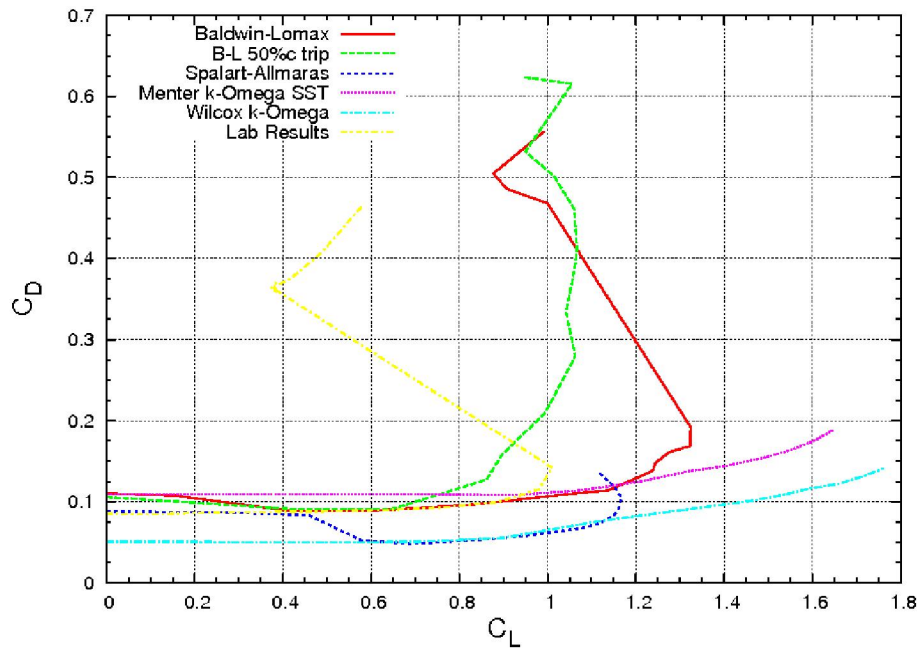
#### 5.4 Turbulence Model Comparison

In order to investigate how much the turbulence models influence the computations for the case of the ellipse, a comparison is made between several turbulence models: (1) Baldwin-Lomax, (2) Spalart-Allmaras, (3) Menter's k-Omega SST model, and (4) Wilcox k-Omega model. In general, the Spalart-Allmaras model is found to perform poorly for this configuration, while the Baldwin-Lomax and Menter's k-Omega SST model perform the best in terms of their ability to predict unsteady behavior.

The time-averaged values of  $C_L$  and  $C_D$  were then plotted for the various turbulence models versus angle of attack (Figure 42). Several observations can be made from the time-averaged  $C_L$  and  $C_D$  plots. First, the values of  $C_L$  for the k-omega models are too high. It is known that the maximum  $C_L$  of the ellipse in the lab is around 1.2 for the baseline case. Also, although the k-omega models have similar values for  $C_L$ , and similar behavior for both  $C_L$  and  $C_D$ , the value of  $C_D$  for Menter's model is nearly double the value of  $C_D$  for the Wilcox model. Also, the values of  $C_D$  for nearly all the models are much higher than expected. Stall also does not occur for the k-omega models or the Spalart-Allmaras model prior to 22 degrees, while the ellipse in the lab stalls somewhere between 16 and 18 degrees for the baseline case. The Baldwin-Lomax and tripped Baldwin-Lomax models stall. However, the stall for Baldwin-Lomax is much more abrupt.



(a)



(b)

Figure 42: Time-averaged  $C_L$  vs.  $\alpha$  and  $C_D$  vs.  $C_L$  for various turbulence models

### 5.4.1 Unsteady Behavior

The time-averaged values of  $C_L$  and  $C_D$ , while useful, do not tell how the coefficients

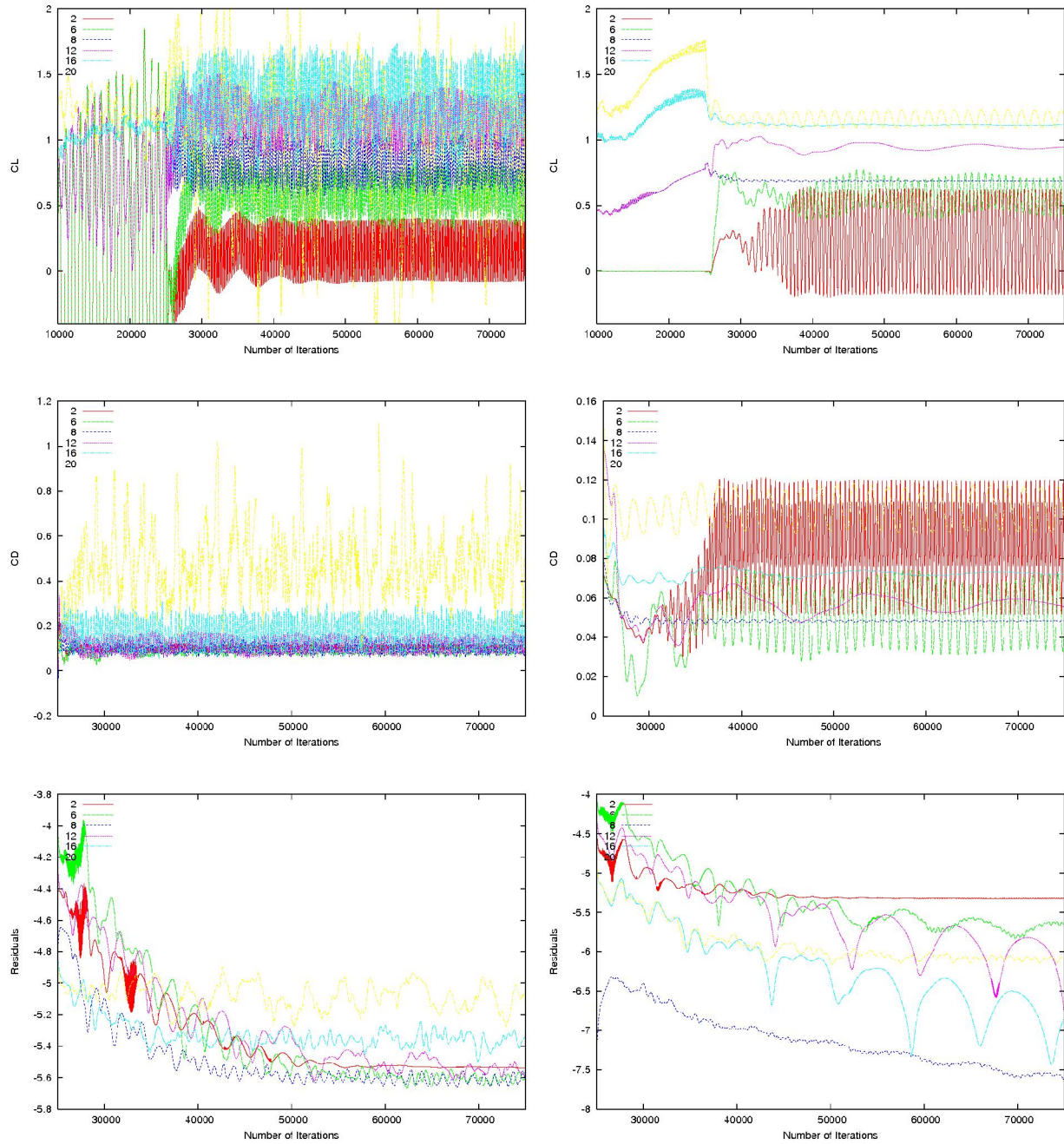
vary with time. Each model has very different time-dependent behavior. So, plots were made showing the time-dependent oscillations in  $C_L$ ,  $C_D$ , and the residuals for varying angles of attack for both the Baldwin-Lomax and Spalart-Allmaras turbulence models (Figure 43).

The Baldwin-Lomax model showed oscillatory results in  $C_L$  at all angles of attack, at frequencies that gradually decrease with angle of attack. And the Baldwin-Lomax solution at 22 degrees was highly oscillatory and noisy, because at this point the ellipse is stalled, and with a value of  $dt = 0.10$  it is assumed that this solution is not very good. The Spalart-Allmaras model was not as consistent, changing from highly oscillatory as zero angle of attack to nearly steady at about 16 degrees, to slightly oscillatory again at 22 degrees. So, there are obviously problems with the Spalart-Allmaras model at varying angles of attack.

Also, the oscillations in  $C_D$  for the Baldwin-Lomax model increase gradually until stall. Note that the scale for the Baldwin-Lomax plot is much higher than for Spalart-Allmaras. This is mostly due to the presence of the stalled solution at 22 degrees. In the Spalart-Allmaras model the time-dependent behavior of  $C_D$  closely mirrors the oscillations in  $C_L$ .

The residuals for the Baldwin-Lomax model exhibit small oscillations. However, at low angles of attack the residuals are nearly steady. This probably occurs because a higher  $dt$  is needed to resolve the solution at higher angles of attack. Also, the residuals for Spalart-Allmaras exhibited the same jumps seen before at about 12 and 16 degrees, where the solution is nearly steady. So, the residuals' jumps are probably a result of the false steady solution computed by the Spalart-Allmaras model.





(a) Baldwin Lomax

(b) Spalart-Allmaras

**Figure 43:  $C_L$ ,  $C_D$ , and the Residuals vs. number of iterations for varying AOAs**

Plots were then made of the Menter and Wilcox k- $\omega$  models. (Figure 44) Although the k- $\omega$  models appear to oscillate at a lower frequency, this is not the case. The axis does not represent time, but the number of iterations. So, the frequency appears 10 times higher because these models run at  $dt = 0.01$  instead of  $dt = 0.10$ . The models also do not begin from

scratch or from a steady run. Because these models are not as robust as others, the previous runs of the Baldwin-Lomax model were used as starting points for the k-omega models. Otherwise, the solution would not converge.

There are obvious differences between the two models. The first is that Menter's model predicts consistent amplitudes of oscillation at various angles of attack. Also, the frequency of oscillations appears to be consistent despite changing the angles of attack. In these respects, its behavior is similar to the Baldwin-Lomax model. The Wilcox model on the other hand predicts steady behavior at an angle of attack of approximately 8 degrees. Again, this suggests a problem in the model. The results should be oscillatory at all angles of attack due to the blunt trailing edge. So, this model is comparable to the Spalart-Allmaras model in its failure to predict oscillations throughout the full range of angles of attack prior to stall.

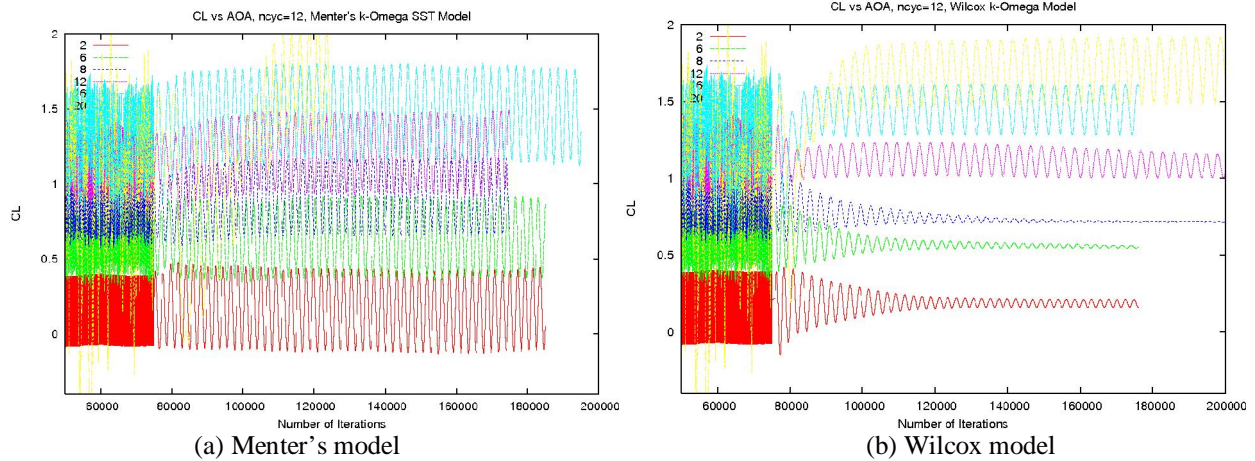


Figure 44:  $C_L$  vs. number of iterations for varying AOAs

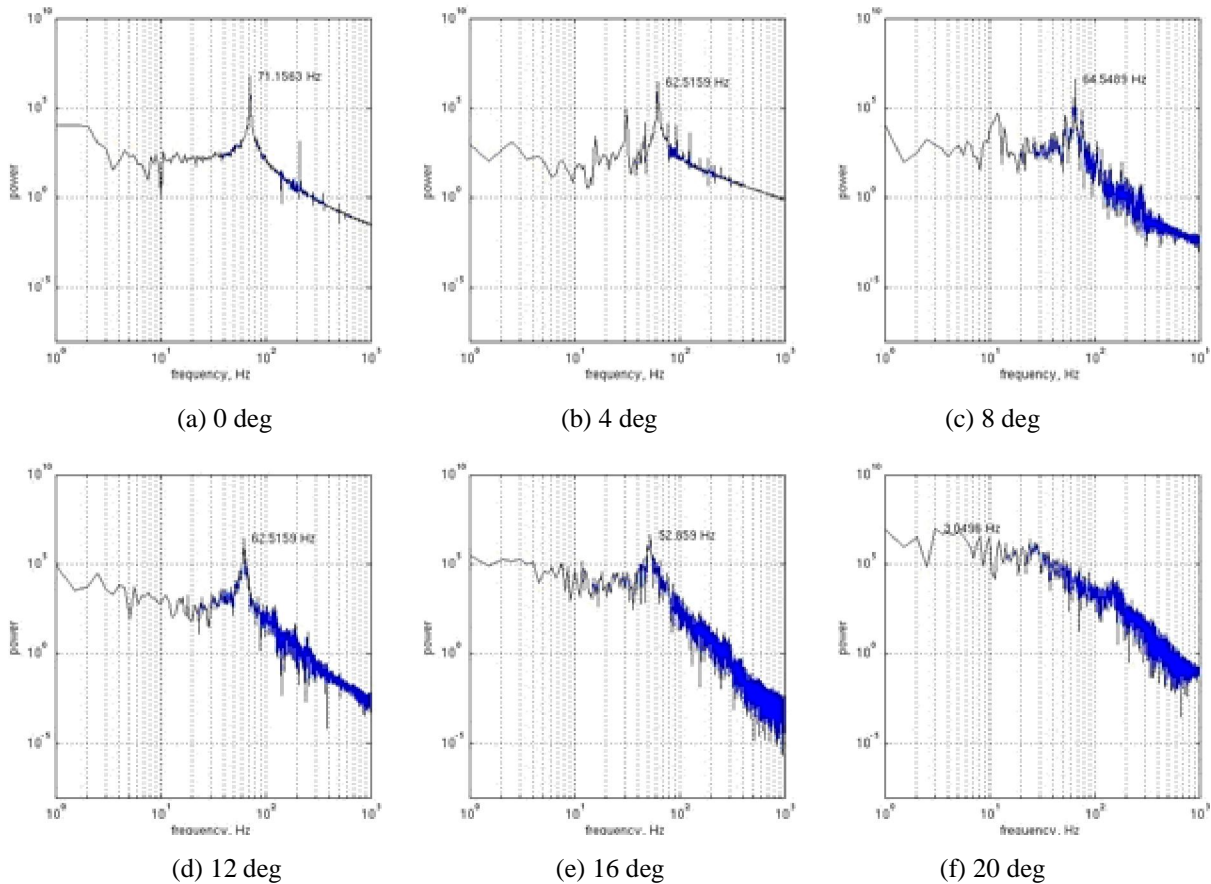
#### 5.4.2 Power Spectrum Analysis

In order to analyze the time-dependent behavior more effectively, especially the frequency of oscillations, power spectra were created using finite Fourier transforms of the time-dependent results. These plots show the dominant frequency of the result, as well as the range of frequencies and the amount of noise. (Figures 45-48) The first observation that can be made from these plots is that the dominant frequency decreases as the angle of attack increases.

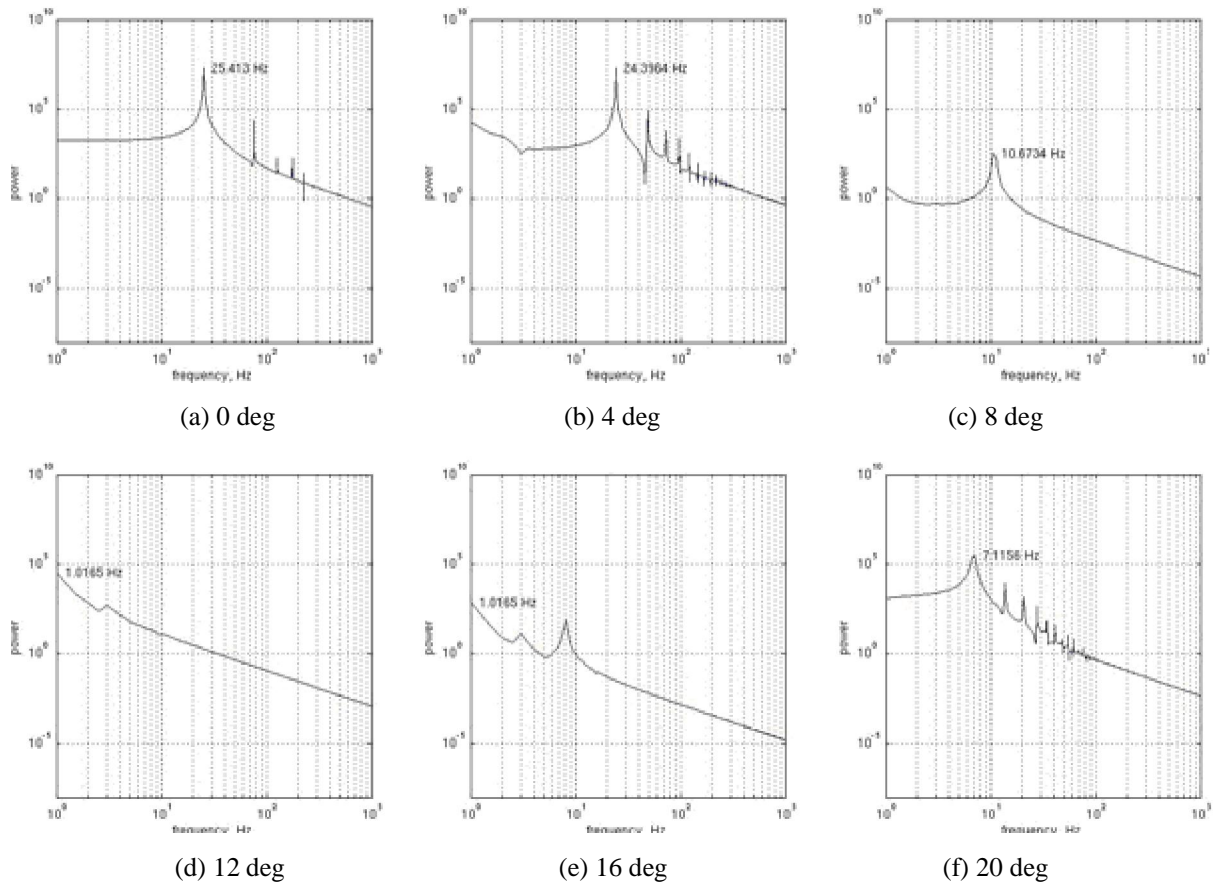


This is due to the fact that as the angle of attack increases the characteristic length should be redefined, and should increase. For example, at 90 degrees angle of attack the characteristic length would be approximately the chord length while at 0 degrees the characteristic length would be the thickness of ellipse. In order to maintain the Strouhal number, the frequency must decrease as the angle of attack (and hence the characteristic length) increases.

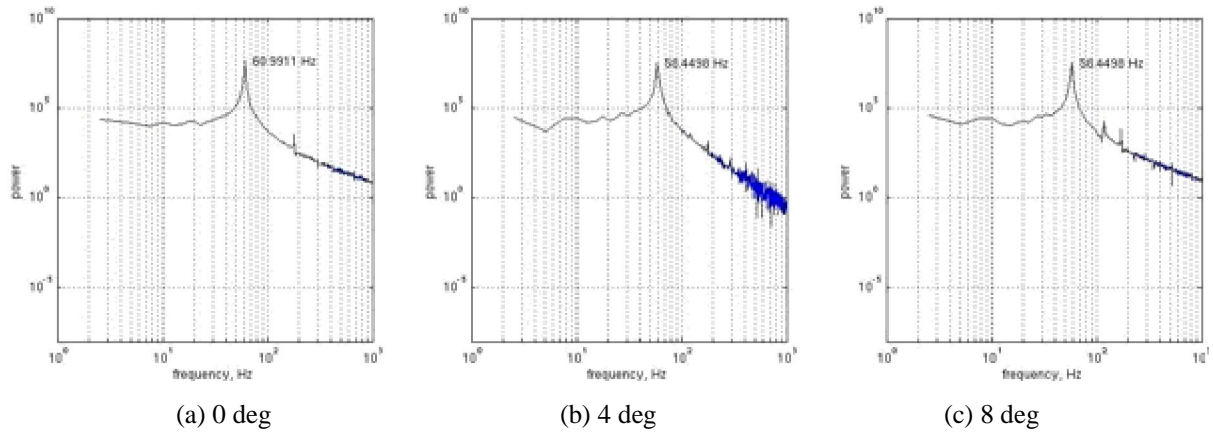
For the Baldwin-Lomax, Menter k-Omega, Wilcox k-Omega and Spalart-Allmaras turbulence models, respectively the dominant frequencies have a range of 71Hz – 52Hz, 61Hz – 51Hz, 56Hz – 38Hz, 25Hz – 7Hz. It is clear once again that the Spalart-Allmaras model is not reaching a viable solution, since the range of frequencies is vastly different from the range of all other turbulence models tested.



**Figure 45: Periodogram for the Baldwin-Lomax Turbulence Model**



**Figure 46: Periodogram for the Spalart-Allmaras Turbulence Model**



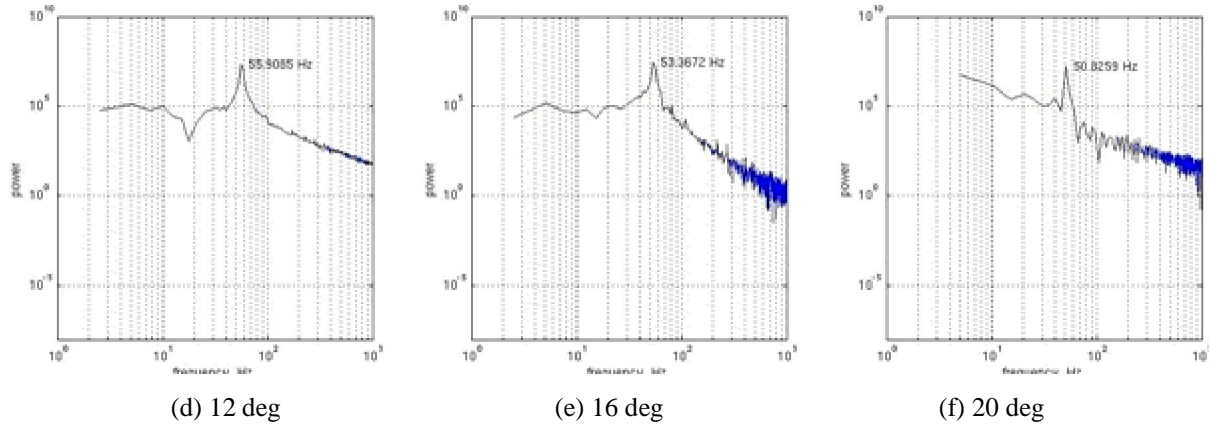


**Figure 47: Periodogram for Menter's k-Omega Turbulence Model**

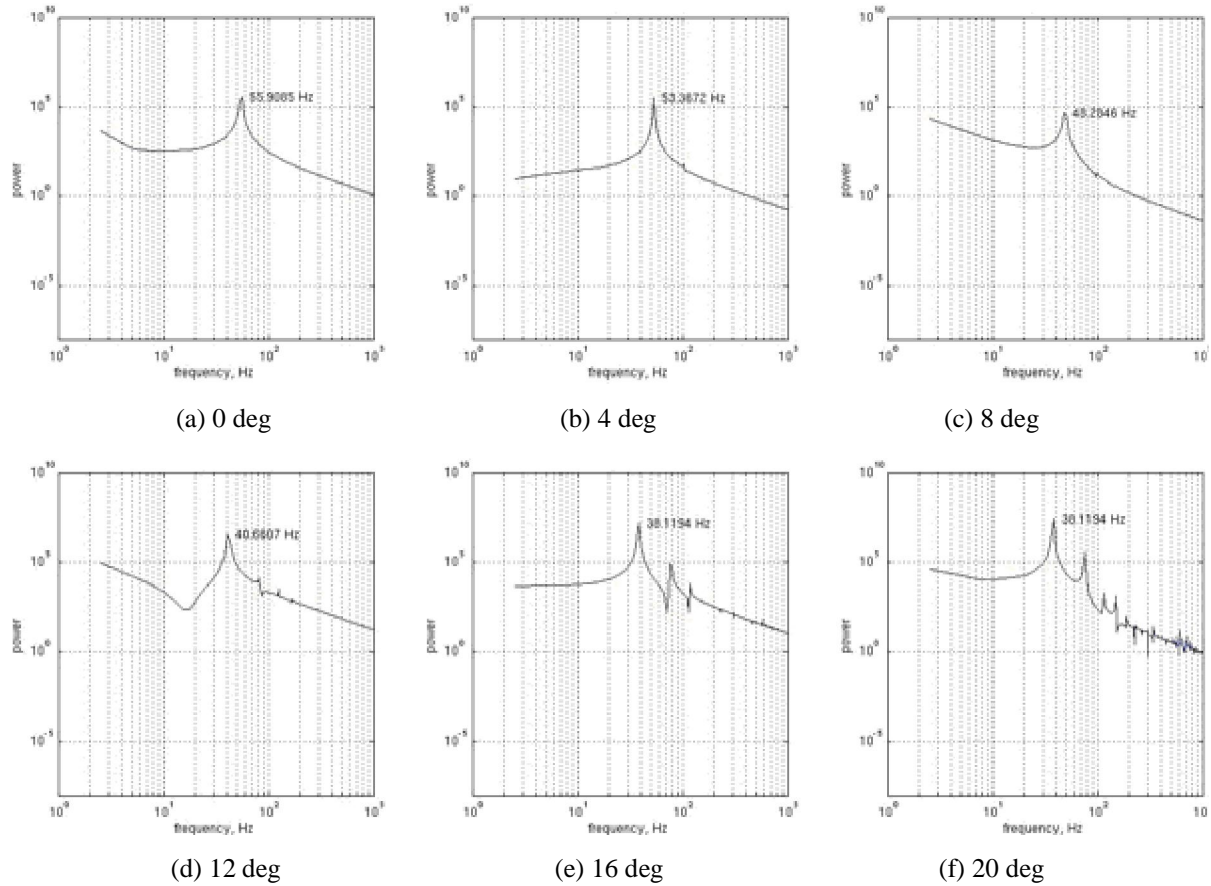


**Figure 48: Periodogram for the Wilcox k-Omega Turbulence Model**

## CHAPTER 6 CONCLUSION

Baseline and active flow control cases for the ellipse were investigated using CFD with the Spalart-Allmaras turbulence model. Overall, it was found that the time averaged lift coefficients predicted by the code were similar to the experimental results. Also, the predicted pressure coefficient along the surface of the ellipse was similar to lab results for the ellipse and the ellipse with the cusp. The negative lift slope curve for the ellipse with the cusp was also well predicted by the code. Also, the results for trailing edge blowing at zero angle of attack were similar to lab results. The maximum negative value of  $C_L$  for blowing downstream was well predicted, as well as the shape of the  $C_L$  vs.  $C_\mu$  curve. And it was found for trailing edge blowing and suction that the value of  $C_L$  was slightly underestimated by the code for the ellipse, and overestimated for the ellipse with the cusp. The hysteresis that occurs when applying leading edge suction was also comparable to the hysteresis found experimentally. The ellipse at 19 degrees would recover from stall at the same value of  $C_\mu$  as it did in the lab. And, the averaged lift and drag coefficients for the stalled and recovered solution were similar to lab results.

Additionally, various turbulence models were tested on the ellipse at angles of attack varying from 0 to 22 degrees. Several issues were found with the solutions generated using the Spalart-Allmaras turbulence model: (1) The model converged to a steady solution at zero angle of attack (2) the solutions were highly dependent on the time step and number of cycles (3) the residuals would make sudden jumps that increased as the solution became more steady (4) the solution would change from unsteady to steady as the angle of attack increased (5) the frequency of oscillations predicted was very poor, whereas all other turbulence models predicted a range of frequencies with reasonable Strouhal numbers. Overall, the Spalart-Allmaras model predicted various flow phenomena with reasonable accuracy, but these accurate predictions were limited to the time averaged values. Of the other models, the most robust solution was the Baldwin-Lomax solution. And, between the Menter and Wilcox k- $\Omega$  model, Menter's model was most able to predict the time-dependent behavior. Also, the Wilcox k- $\Omega$  model displayed similar issues with the time dependent behavior as the Spalart-Allmaras model.

## BIBLIOGRAPHY

- [1] Hoerner, S. F., "Fluid-Dynamic Lift," Hoerner Fluid Dynamics, Bakersfield, 1985.
- [2] White, F. M., "Viscous Fluid Flow," McGraw-Hill Inc., New York, 1974.
- [3] Launder, B. E., and Spalding, D. B., "Lectures in Mathematical Models of Turbulence," Academic Press Inc., New York, 1972.
- [4] Bachelor, G. K., "An Introduction to Fluid Dynamics," Cambridge Univ. Press, Cambridge, England, 1967.
- [5] Baldwin, B. S., Lomax, H., "Thin Layer Approximation and Algebraic Model for Separated Turbulent Flows," AIAA-78-257, 1978.
- [6] Spalart, P. R., and Allmaras, S. R., "A One-Equation Turbulence Transport Model for High Reynolds Number Wall-Bounded Flows," NASA-TM-102847, 1990.
- [7] Wilcox, D. C., "Turbulence Modeling for CFD," 2<sup>nd</sup> Edition, La Canada, California: DCW Industries, Inc., 1998.
- [8] Menter, F. R., "Improved Two-Equation  $k - \omega$  Turbulence Models for Aerodynamics Flows," NASA-TM-103975, 1992.
- [9] Chen, C., Zakharin, B., and Wagnanski, I., "On the Parameters Governing Fluidic Control of Separation and Circulation," AIAA-2008-629, 2008.
- [10] Potsdam, M. and Le Pape, A., "CFD Investigations on a NACA0036 Airfoil with Active Flow Control," AIAA-2008-3869, 2008.
- [11] Nishri, B. and Wagnanski, I., "Effects of Periodic Excitation on Turbulent Flow Separation from a Flap," *AIAA Journal*, Vol. 36, No. 4, 1998.
- [12] Bartels, R. E., Rumsey, C. L. and Biedron, R. T., "CFL3D Version 6.4 – General Usage and Aeroelastic Analysis," NASA-TM-2006-214301, 2006.
- [13] Chan, W. M., "The Overgrid Interface for Computational Simulations on Overset Grids," AIAA-2002-3188, 2002.
- [14] Biedron, R. T. and Rumsey, C. L., "CFL3D User's Manual Version 5.0," NASA-TM-1998-208444, 1998.
- [15] Chan, W., Chiu, I. and Buning, P., "User's Manual for the HYPGEN Hyperbolic Grid Generator and the HGUI Graphical User Interface," NASA-TM-1993-108791, 1993.

- [16] Sivasubramanian, J., “Numerical Simulation of Flow Past an Elliptical Section with Active Flow Control,” (MS thesis, The University of Arizona, 2003).